ADVANCING EARTH AND SPACE SCIENCE

Geochemistry, Geophysics, Geosystems

RESEARCH ARTICLE

10.1029/2020GC009428

Antarctic Geothermal Heat Flow Model: Aq1

Tobias Stål[1,2], Anya M. Reading[1,2], Jacqueline A. Halpin[2], and Joanne M. Whittaker[2]

[1]School of Natural Sciences (Earth Sciences/Physics), University of Tasmania, Hobart, TAS, Australia, [2]Institute for Marine and Antarctic Studies, University of Tasmania, Hobart, TAS, Australia

Key Points:

- A new heat flow map of Antarctica suitable for solid Earth and interdisciplinary studies is presented
- Multiple observables are combined in a similarity approach to link global data compilations
- A reproducible, adaptable workflow with uncertainty metrics is provided

Supporting Information:

- Supporting Information S1

Correspondence to:

T. Stål,
tobias.staal@utas.edu.au

Citation:

Stål, T., Reading, A. M., Halpin, J. A., & Whittaker, J. M. (2021). Antarctic geothermal heat flow model: Aq1. *Geochemistry, Geophysics, Geosystems*, *22*, e2020GC009428. https://doi.org/10.1029/2020GC009428

Received 11 SEP 2020
Accepted 5 DEC 2020

Abstract

We present a refined map of geothermal heat flow for Antarctica, Aq1, based on multiple observables. The map is generated using a similarity detection approach by attributing observables from geophysics and geology to a large number of high-quality heat flow values ($N = 5{,}792$) from other continents. Observables from global, continental, and regional datasets for Antarctica are used with a weighting function that allows the degree of similarity to increase with proximity and how similar the observables are. The similarity detection parameters are optimized through cross correlation. For each grid cell in Antarctica, a weighted average heat flow value and uncertainty metrics are calculated. The Aq1 model provides higher spatial resolution in comparison to previous results. High heat flow is shown in the Thwaites Glacier region, with local values over 150 mW m^{-2}. We also map elevated values over 80 mW m^{-2} in Palmer Land, Marie Byrd Land, Victoria Land and Queen Mary Land. Very low heat flow is shown in the interior of Wilkes Land and Coats Land, with values under 40 mW m^{-2}. We anticipate that the new geothermal heat flow map, Aq1, and its uncertainty bounds will find extended use in providing boundary conditions for ice sheet modeling and understanding the interactions between the cryosphere and solid Earth. The computational framework and open architecture allow for the model to be reproduced, adapted and updated with additional data, or model subsets to be output at higher resolution for regional studies.

Plain Language Summary

We present a new map that shows how the heat from the deep Earth varies from place to place in Antarctica. The map shows where raised heat flow values beneath ice sheets need to be included to better predict how ice sheets will respond to the Earth's warming climate. Areas with volcanoes have high geothermal heat flow. Other medium to high heat flow locations are often hard to identify, especially as it is too difficult or expensive to measure the heat directly in the harsh and sensitive Antarctic environment. To overcome this challenge, we use a technique with computer-aided match between the best data we can compile for Antarctica and corresponding data and heat flow values from other continents.

1. Introduction

The distribution of continental heat flow is the result of Earth's dynamic processes through geological time: ongoing tectonic processes bring hot material to the surface, and enhance the local geothermal gradient; past tectonic processes distributed heat producing elements unevenly in the crust; exhumation and deposition controls the geothermal heat transfer on local, regional, and continental scales. Subglacial geothermal heat in Antarctica has significance for studies of the tectonic history (Artemieva, 2011), and has also been identified as a boundary condition for ice sheet models (Matsuoka et al., 2012; Pattyn, 2010; Pattyn et al., 2016; Pittard et al., 2016; Van Liefferinge et al., 2018; Whitehouse et al., 2019; Winkelmann et al., 2011). Understanding the response of the Antarctic ice sheets to changing climate, and improving the prediction of related contributions to global sea level, is of highest importance (DeConto & Pollard, 2016; Golledge et al., 2015). Due to limited geological data, and lack of values based on direct measurements, heat flow is difficult to constrain in the Antarctic interior, and existing maps have appreciable differences between them (discussed by, e.g., Burton-Johnson et al., 2020; Stål et al., 2020). The need for better estimates encourage us to develop methods to best constrain the spatial variation of heat flow using available data, while accepting that the uncertainties remain large. In this contribution, we present Aq1, a new approach to estimate Antarctic heat flow (Figure 1).

10.1029/2020GC009428

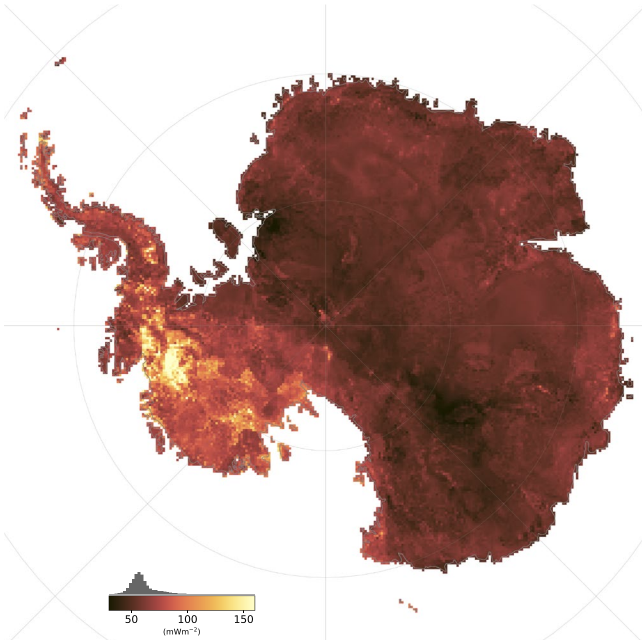

Figure 1. Heat flow map of Antarctica, Aq1.

The few direct heat flow estimates across interior Antarctica have been made using measurements from the base of the ice sheet rather than in bedrock, as is typical on other continents. These subglacial measurements suggest high spatial variability and complex hydrological interaction between the cryosphere and solid Earth (Begeman et al., 2017; Fisher et al., 2015; Wright et al., 2012). Thermal gradients within the ice can provide insight for ice sheet models and models of subglacial hydrology (Price et al., 2002), but cannot be used to estimate the solid Earth contribution with any certainty, unless the exact conditions at the base are known, or assumed, and the borehole reaches sufficient depth (Mony et al., 2020; Tulaczyk et al., 2001). Constraints for subglacial heat flow can also be inferred from thermomechanical ice-flow models (e.g., MacGregor et al., 2016; Pattyn, 2010; Van Liefferinge et al., 2018), or mapping of subglacial lakes (e.g., Pattyn et al., 2016). Such models show the general trends in expected heat transfer, and also suggest large regional and local variability. Crustal geothermal heat flow is difficult to separate from the impact of basal friction of fast flowing glaciers (Larour et al., 2012; Pattyn, 2010), the energy needed for melting ice (Fudge et al., 2013), or advection by ground water that occurs in sediment layers or other permeable rocks beneath (Siegert et al., 2016).

An alternative to calculating heat flow values from field measurements is to derive a temperature gradient using indirect methods applied to geophysical data, and calculate the resulting heat flow (An et al., 2015b; Fox Maule et al., 2005; Martos et al., 2017; Purucker, 2012). These methods are associated with large uncertainties regarding how well the temperature and depth are constrained (discussed by e.g., Haeger et al., 2019; Burton-Johnson et al., 2020; Lösing et al., 2020; Stål et al., 2020). Studies that rely on the temperature in the lower crust or upper mantle also depend on assumptions regarding the 3D distribution of heat production and thermal conductivity in the crust, and shallow transient heat sources (e.g., Artemieva & Mooney, 2001; Jaupart et al., 2016). Shapiro and Ritzwoller (2004) used a global seismic model to match heat flow records in a global compilation (Pollack et al., 1993) to assign heat flow values in Antarctica. With this approach a realistic range of the crustal contribution is captured, noting that the result depends on how the low-resolution seismic wave speed data of the lithosphere captures variations in the crust. Using recent seismic tomography models from Shen et al. (2018) and Lloyd et al. (2020), and heat flow estimates in continental US, Shen et al. (2020) used similar approach to generate a heat flow map of higher resolution and defined uncertainty bounds. This body of work significantly progressed the understanding of particularly the thermal properties of West Antarctica, and accords to a great extent with the recently reviewed geological history (Jordan et al., 2020).

A large fraction of the heat flow originates from radioactive decay of elements within enriched material in the crust (e.g., Artemieva & Mooney, 2001; Hasterok & Chapman, 2011; Jaupart & Mareschal, 2014), and considering the crust can therefore substantially improve heat flow maps. Reviews suggest a general correlation between observed heat production and heat flow, but this relationship is not universal (e.g., Jaupart et al., 2016; Levy et al., 2010; McLaren et al., 2003). Studies of heat production in crustal rocks (e.g., Carson et al., 2014; Goodge, 2018) provide us with a first insight into the variability of heat production in Antarctica. Heat production in rocks has a weak correlation with thermal age and is informed by geochemical composition (e.g., Hasterok et al., 2018; Hasterok & Webb, 2017; Jaupart & Mareschal, 2014), but such properties are to a large extent unknown in the subglacial interior. Burton-Johnson et al. (2017) provided a detailed study for the Antarctic Peninsula with heat production in the upper crust assigned from limited extrapolation of geological and geochemical observations. This study suggested that crustal heat production accounts for 6%–70% of the total heat flow. However, such studies cannot be performed on a continental scale as over 99.8% of Antarctica is unexposed (Burton-Johnson et al., 2016). A steady state Antarctic geothermal heat flow model, AqSS (Stål et al., 2020), uses a constant mantle heat flow component and introduces a first order approach for integrating heterogeneous heat production within segmented crust. Heat that is not generated by crustal heat production or heat flow across the Moho, must be associated to dynamic and

10.1029/2020GC009428

transient heat transfer by ongoing tectonics or shallow processes. Significant differences between estimates from available Antarctic heat flow models and this steady state model, AqSS, can therefore indicate regions with such conditions.

Heat flow studies for Antarctica's neighbors prior to the breakup of Gondwana (e.g., McLaren et al., 2003; Pollett et al., 2019; Roy & Rao, 2003; Rudnick & Nyblade, 1999), and the continental shelf (e.g., Dziadek et al., 2017; Morin et al., 2010) suggest the nature of heterogeneity of heat flow to expect in Antarctica. However, extrapolations must be treated with caution due to the high spatial variability of heat flow (e.g., Carson et al., 2014; Jaupart & Mareschal, 2014), and limited extent of shared coastal domains (e.g., Aitken et al., 2014; Maritati et al., 2019; Stål et al., 2019; Tucker et al., 2017). Cenozoic processes of deposition and exhumation have a different history in domains that were recently separated at Gondwana breakup, as seen in the asymmetric distribution of terrigenous sedimentation in the marine environment between the Australian and the Antarctic margins (e.g., Sauermilch et al., 2019). Sedimentation, erosion and exhumation have large impact on heat flow (Beardsmore & Cull, 2001; England & Richardson, 1980; Jessop & Majorowicz, 1994), but are still poorly constrained in the Antarctic interior, and is the subject of ongoing work (e.g., Paxman et al., 2019).

A much greater number of estimates of heat flow from in situ thermal gradient and conductivity measurements exist for continents other than Antarctica. Motivation for those measurements includes studies underpinning hydrocarbon reservoirs, geothermal energy, structural studies for potential mineral exploration, and understanding of Earth's energy balance and age (Beardsmore & Cull, 2001). The research area has been facilitated by cumulative compilations (e.g., Hasterok, 2019; Lucazeau, 2019; Pollack et al., 1993). Measurements are, however, irregular in distribution, and are of variable quality. To improve interpolation, Goutorbe et al. (2011) developed a similarity method where heat flow is linked to geological and geophysical observables. A heat flow value for a given location is derived from measurements with a similar geological context. When a number of observables combined suggests a heat flow value within a given range, this is more robust than a heat flow value constrained by only one data set. Lucazeau (2019) applied the method to a larger number of measurements from the New Global Heat Flow database (NGHF). In this study, using 14–19 sets of observables produces a misfit of less than 10 mW m^{-2}, and a larger number of datasets does not improve the estimates significantly yet risks the introduction of noise. Observables as crustal type, age, and sediment thickness provide robust constraints to link heat flow measurements to target locations. However, such datasets are not available for the subglacial interior of Antarctica and this method must therefore be adapted for application with a limited range of observables.

Our new model, Aq1, uses a modification of the similarity approach employed by Goutorbe et al. (2011) to infer Antarctic heat flow from global comparisons. We also provide uncertainty metrics to inform the interpretation of the resulting map and its further use. The Aq1 model is provided with a computational framework to facilitate generation of, e.g., refined regional studies and include future datasets (discussed by Stål et al. [2020).

2. Data

In the following section we describe the datasets used in the study, and any necessary initial data preparation.

2.1. Heat Flow Data

New Global Heat Flow is an extended compilation of earlier heat flow catalogs, associated with meta data attributes with links to original studies (Lucazeau, 2019). We exclude records in the case of missing coordinates, missing heat flow values, and a few high latitude measurements, where map distortion might impact some observables used (Figure S1a). In order to remove records from deep oceans, but keep those on continental shelves and measurements at depths representing the low hypsometry of West Antarctica (e.g., Artemieva & Thybo, 2020; Morlighem et al., 2019), we exclude measurements deeper than 1,000 m below sea level (Table 1 and supplementary material Figure S1b). The quality of heat flow measurements is rated in NGHF. The rating category for each measurement is based on, e.g., the variation of heat flow in the bore-

Table 1
Heat Flow Records in NGHF

N	Filtering	Min[a] mW m^{-2}	Max mW m^{-2}	Average mW m^{-2}	Median mW m^{-2}
69,729	All records	−401.0	72,000	120.5	62
69,377	Excluded incomplete records	−401.0	72,000	120.5	62
46,270	Excluded deeper than 1,000 m bsl	−401.0	15,600	99.6	62
46,113	Excluded high latitudes	−401.0	15,600	99.6	62
35,647	Rating A[b], B[c], C[d]	−3.0	15,600	101.1	61
12,707	Rating A[b], B[c]	−3.0	5,146	66.1	59
5,792	Rating A[b]	0.8	787.5	65.8	59

Number of records after cleaning of data.
[a]Negative value would here indicate heat flow into the Earth. [b]Best rating, e.g., defined as 10% variation in measurement. [c]Good rating, e.g., up to 20% variation in measurement. [d]Average rating, e.g., up to 30% variation in measurement.

hole where the measurement is performed. Old and questionable measurements are generally assigned a lower rating. When removing lower rated heat flow measurements, the mean value decreases (Table 1). This is a consequence of removal of a small number of high values from locations with geothermal activity. The median of the heat flow data remains within 3 mW m^{-2}. The distribution of heat flow values, before and after removal of records as above, is provided in Figure S1a. We include only records rated A. For reference, we also provide a version where also *B*-rated records are used (Figure S2). Including lower rated records generates a similar overall structure and significantly increases the uncertainty range of the model.

2.2. Observables

We refer to associated data, models, and distances as observables, i.e., this term is used in a broad sense. Reference observables (o_R) are linked to each listing in the heat flow catalog (NGHF, Lucazeau, 2019), and target observables (o_T) are linked to each 2D grid cell for our Antarctic model. When provided, we include uncertainty estimates to guide the similarity analysis. For most of Antarctica, we are limited to datasets derived from satellite potential field measurements and large-scale seismology. For outcrops along the coast and Transantarctic Mountains, we access petrological data from previous studies and compilations (Gard et al., 2019), and take advantage of geological experience, and extrapolation (Hartmann & Moosdorf, 2012; Tingey et al., 1991). Additional information has been derived from existing datasets, for example, subglacial topographic shapes (e.g., van Wyk de Vries et al., 2018) and curvature in the gravitational field (e.g., Ebbing et al., 2018).

Eighteen pairs of observables are included to match heat flow measurements with Antarctic continental properties (Table 2 and Figure S3). Each observable is contributing to a decrease of cross-validated root mean squared error (RMSe) and mean absolute error (MAe) for heat flow measurements in NGHF (Figure S4). Reference observables are also plotted against measured heat flow in Figure 2 and maps of a selection of observables are given (Figure S5). The four types of observables are processed differently; continuous data, sparse data, classes, and distance functions.

2.2.1. Continuous data

Continuous data cover most of the Antarctic continent and consist of satellite and airborne geophysical measurements, seismic tomography, and elevation data. Global models often lack resolution and accuracy in Antarctica (e.g., Figure S6). Where available, we use Antarctic studies as target observables. Global Moho depth is provided from Szwillus et al. (2019). The model is similar to CRUST1 (Laske et al., 2013), but has refined, transparent interpolation, and well-defined uncertainty bounds. In Antarctica, we use AN_CRUST

10.1029/2020GC009428

Table 2
Observables Used in This Study

	Observable(s) (label o_R in Figure 2)	Weighting function, w
	Reference observable, o_R	Similarity range, σ_R
	Target observable, o_T	Similarity range, σ_T
Continuous	*Moho Depth (a)*	
	o_R: Szwillus et al. (2019)	σ_R as provided
	o_T: An et al. (2015a)	$\sigma_T = 1.0$ km
	LAB Depth (b)	
	o_R: Afonso et al. (2019)	$\sigma_R = 18$ km
	o_T: An et al. (2015b)	$\sigma_T = 18$ km
	Lithospheric Mantle Thickness (c)	
	o_R: LAB depth—Moho depth[a]	$\sigma_R = 20$ km
	o_T: LAB depth—Moho depth[a]	$\sigma_T = 20$ km
	Shear Wave Speed, Versus 125 km	
	o_R: Becker and Boschi (2002)	$\sigma_T = 1.50\%$
	o_T: Becker and Boschi (2002)	$\sigma_T = 1.50\%$
	Pressure Wave Speed, Vp 150 km (e)	
	o_R: Becker and Boschi (2002)	$\sigma_R = 0.25\%$
	o_T: Becker and Boschi (2002)	$\sigma_T = 0.25\%$
	Curie Temperature Depth (f)	
	o_R: Li et al. (2017)	$\sigma_T = 4$ km
	o_T: Martos et al. (2017)	σ_T as provided
	Earth Magnetic Anomaly (g)[a]	
	o_R: Meyer et al. (2016)	$\sigma_R = 0.06$[a]
	o_T: Golynsky et al. (2018)	$\sigma_T = 0.06$[a]
	Elevation (h)	
	o_R: Amante and Eakins (2009)	$\sigma_R = 275$ m
	o_T: Morlighem et al. (2019)[a]	σ_T as provided
	Lithosphere Average Density (i)	
	o_R: Afonso et al. (2019)	$\sigma_R = 12$ kg/m^3
	o_T: Ibid.	$\sigma_T = 12$ kg/m^3
	Crustal Average Density (j)	
	o_R: Afonso et al. (2019)	$\sigma_R = 36$ kg/m^3
	o_T: Afonso et al. (2019)	$\sigma_T = 36$ kg/m^3
	Free Air Gravity (k)	
	o_R: Förste et al. (2013)	$\sigma_T = 0.0075$ mGal
	o_T: Förste et al. (2013)	$\sigma_T = 0.0075$ mGal
	Geoid Height (l)	
	o_R: Förste et al. (2013)	$\sigma_R = 8$ m
	o_T: Förste et al. (2013)	$\sigma_T = 8$ m
	Bouguer Gravity Anomaly (m)	
	o_R: Sinem Ince et al. (2019)	$\sigma_R = 0.03$ mGal
	o_T: Scheinert et al. (2016)	$\sigma_T = 0.03$ mGal

Table 2
Continued

	Observable(s) (label o_R in Figure 2) / Reference observable, o_R / Target observable, o_T	Weighting function, w / Similarity range, σ_R / Similarity range, σ_T
	Shape Index of Curvature (n)	
	o_R: Ebbing et al. (2018)	$\sigma_R = 1/8$
	o_T: Ebbing et al. (2018)	$\sigma_T = 1/8$
Class	*Tectonic Regionalization (o)*	
	o_R: Schaeffer and Lebedev (2015)	Identical only
	o_T: Schaeffer and Lebedev (2015)	Identical only
	Global Lithological Map (P)	
	o_R: Hartmann and Moosdorf (2012)	Identical only
	o_T: Hartmann and Moosdorf (2012)	Identical only
Sparse	Heat production (q)	$w = 1$ −obs/250 km
	o_R: Gard et al. (2019)[a,b]	$\sigma_R = 0.5\ \mu\mathrm{Wm}^{-3}$
	o_T: Gard et al. (2019)	$\sigma_T = 0.5\ \mu\mathrm{Wm}^{-3}$
Dist.	Distance-to-nearest volcano (r)	$w = 1$ −obs/100 km
	o_R: Global Volcanism Program (2013)	$\sigma_R = 25$ km
	o_T: Ibid. van Wyk de Vries et al. (2018)	$\sigma_T = 25$ km

Note. The content is discussed in the text.
[a]Details provided in text. [b]And references therein.

(An et al., 2015a) as the matching target observable. Both observables refer to Moho depth, but AN_CRUST has higher resolution and is generated from surface wave tomography and constrained by available regional receiver function studies (Figure S5a). Similarly, we use the global Lithosphere-Asthenosphere boundary (LAB) from Afonso et al. (2019), and the model AN_LAB from An et al. (2015a) in Antarctica (Figure S5b). Thickness of lithospheric mantle is calculated as the difference between LAB depth, and Moho depth (Afonso et al., 2019). Depth to Curie temperature is derived from magnetic data. Reference observables are from GCDM (Li et al., 2017) using data from EMAG2 (Maus et al., 2009). In Antarctica, GCDM has limited cover, and we use CTD from Martos et al. (2017) with provided uncertainty bounds (Figure S5c). We use the EMAG2v3 magnetic anomaly map from Maus et al. (2009) and Meyer et al. (2016) as a separate reference observable and ADMAP2 (Golynsky et al., 2018) as a target observable, noting that EMAG2v3 and ADMAP2 only rely on observed data. As magnetic anomalies vary over several orders of magnitude, we apply a logarithmic function that preserves the sign: $M_{\log} = \mathrm{sgn}(M) \times \ln(1 + M/400)$, clipped to range $[-1, 1]$, where M is the linear data and $M_{\log}$ the rescaled observable. Our reference digital elevation model is ETOPO1 (Amante & Eakins, 2009), and in Antarctica we use the subglacial topography from MEaSUREs BedMachine (Morlighem et al., 2019), with uncertainty bounds. A simplistic glacial isostatic adjustment (GIA) correction is performed for total ice loading relaxation (Stål et al., 2020), using an ice density of 917 kgm^{-3} (Griggs & Bamber, 2011) and crustal, and lithospheric mantle densities from Afonso et al. (2019). Crustal and lithospheric thickness to estimate GIA are obtained from An et al. (2015a, 2015b). We apply a simplified flexural model as a Gaussian kernel of $\sigma = 60$ km. For this context, we chose not to correct for global sea level adjustment, as it would also impact coastal reference observables (Figure S7). By using the interpolated mean elevation for each cell, we remove most topographic effects on heat that depend on the roughness (Lees, 1910) as those are beyond the resolution of the target observable for most of Antarctica (Graham et al., 2017). Four aspects of the gravity field are included as observables, all derived from EIGEN-6C4 model (Förste et al., 2013). Computations of geoid, free air gravity and Bouger gravity are performed by ICGEM (Drewes et al., 2016; Sinem Ince et al., 2019) and provide a global, reliable frame covering the whole Antarctic continent. The Bouguer gravity reference observable includes ETOPO1 (Amante &

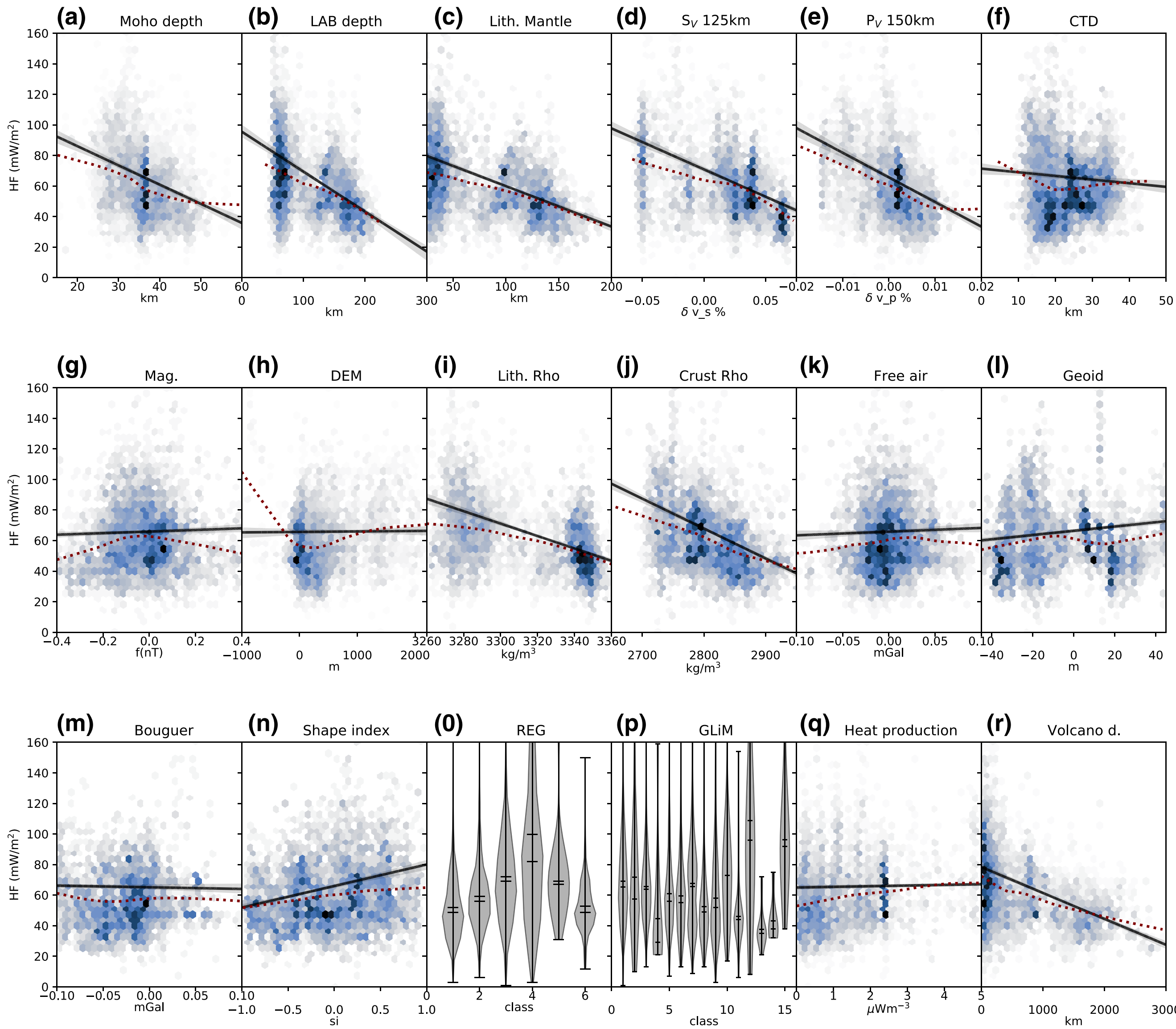

Figure 2. Cross plots of reference observables (O_R) and used heat flow records from NGHF (Lucazeau, 2019), as described in the text. Observable value and heat flow value are binned to a hexagonal grid, where the color represent the relative frequency of heat flow values. Classes are shown as violin plots with the distribution of heat flow measurements for each class. Linear regression (black line) highlights any general relation between observable and heat flow. A nonparametric locally weighted scatterplot smoothing (LOWESS) is plotted as dotted red line (Cleveland, 1979; Waskom et al., 2020). (a) Moho depth (Szwillus et al., 2019), (b) Lithosphere thickness (Afonso et al., 2019), (c) Thickness of lithospheric mantle (Afonso et al., 2019; Szwillus et al., 2019), (d) Shear wave speed at 125 km (SMEAN2 (2016) based on Becker & Boschi, 2002), (e) Pressure wave speed at 150 km (Becker & Boschi, 2002), (f) Curie temperature depth (Li et al., 2017), (g) Magnetic anomalies (Maus et al., 2009; Meyer et al., 2016), (h) Elevation (ETOPO1 Amante & Eakins, 2009), (i) Lithosphere average density (Afonso et al., 2019), (j) Crustal average density (Afonso et al., 2019), (i) Free air gravity anomalies (Förste et al., 2013; Sinem Ince et al., 2019), (j) Geoid height (Förste et al., 2013; Sinem Ince et al., 2019), (k) Bouguer anomaly (Förste et al., 2013; Sinem Ince et al., 2019), (l) Shape index of satellite gravity gradients (Ebbing et al., 2018), (m) Tectonic regionalization classes (Schaeffer & Lebedev, 2015), (n) Lithological data classes (Hartmann & Moosdorf, 2012), (o) Heat production (Gard et al., 2019), (p) Distance-to-nearest volcano (Global Volcanism Program, 2013). Examples of datasets are presented in more details in supplementary material Figure S5, and discussed in text.

Eakins, 2009). Global compilations of Bouguer corrected gravity field are not valid in ice covered areas. For Antarctica, we therefore use the Bouguer gravity model from Scheinert et al. (2016). This model covers 73% of the continent with gravity data from airborne surveys and topography model from BEDMAP2 (Fretwell et al., 2012). We also include the shape index of curvature of gravity field (Ebbing et al., 2018) from GOCE data (Pail et al., 2010) (Figure S5d).

2.2.2. Discrete Class Data

We use the tectonic segmentation of Schaeffer and Lebedev (2015). This is a robust global segmentation, but it is produced in low resolution. We note that in some locations, particularly along the circumference of Antarctica, this segmentation does not agree with geological and regional geophysical studies. Projection artifacts are mitigated using a median filter, with a 111 km × 111 km circular kernel. We also include geological classification, including reasonable extrapolation of geological observations in Antarctica from the GLiM compilation (Hartmann & Moosdorf, 2012; Tingey et al., 1991). We exclude the classes for Water Bodies (wb), Ice and Glaciers (ig), and No Data (nd). With those classes removed, only 11% of the Antarctic continent is classified, mainly in West Antarctica, along the coast, and Transantarctic Mountains.

2.2.3. Sparse Data

Estimates of heat production from geochemistry are taken from the compilation by Gard et al. (2019). The median heat production value and uncertainty for each grid cell are interpolated to nearest observation over unrealistic long distances, but are assigned a weighting function that decreases linearly over 250 km, as described below. We reduce errors in the sparse target observable by excluding reported observations not consistent with exposed outcrops (Burton-Johnson et al., 2016).

2.2.4. Distance functions

Distance to phenomena that have an impact on heat flow are also included. Distances to nearest Holocene and Pleistocene volcano are calculated from global compilation by Global Volcanism Program (2013). In addition, as an Antarctic observable, we also include subglacial volcanoes suggested by van Wyk de Vries et al. (2018) with total quality rating over 2.5. All volcanoes in the list are suggested to be shield volcanoes, as defined by the morphology (Grosse et al., 2014). It could have been beneficial for our purposes to separate Holocene and Pleistocene volcanism, but as we do not have this information for the subglacial volcanoes, we treat those reference observables equally. Distances are calculated along the great circle using *pyproj*, a PROJ4 package for Python (Snow et al., 2020).

2.3. Data Preparation

Using *agrid* (Stål & Reading, 2020), we setup a global multivariate grid to import reference observables, in WGS 1984 (epsg:4326), with a resolution of 0.2 × 0.2°. We exclude the few values south of 60°S and north of 80°N to avoid distortion as previously noted. For continuous data, a bi-linear interpolation of the cell center is obtained. For classes, we use the nearest value to each cell center. Heat production values are included as median of all records in each cell. Distance (in km) to the nearest Holocene and Pleistocene volcano (Global Volcanism Program, 2013) is assigned to each heat flow record.

To extract continuous data for the locations of heat flow measurements, we identify the nearest grid cells and generate an index matrix using KD-tree (Bentley, 1975). The index matrix is used to extract interpolated values from reference observables at the location of the heat flow measurement. The average distance between heat flow measurements and nearest grid center is 7.6 km, the maximum distance is 15.6 km (Figure S8). We also extract provided uncertainty bounds for continuous data, where available.

An Antarctic grid is generated (similar to Stål et al., 2020). The grid is in 20 × 20 km resolution, with an extent of 5,600 × 5,600 km in WGS 84/Antarctic Polar Stereographic (epsg:3031). We also set up a grid in 50 × 50 km resolution (Figure S9). We limit the model to the coastline and grounding line (Mouginot, Scheuchl, & Rignot, 2017). Target observables are listed in Table 2. We also construct a grid to generate a test heat flow map for Australia, as a comparison of the potential, and limitations, of the methodology and observables used (Figure S18).

3. Methods

Data handling and other stages of the workflow are coded in Python, using packages including *agrid* (Stål & Reading, 2020), *numpy* (Harris et al., 2020), *pandas* (McKinney, 2015), and *scipy* (Jones et al., 2015). Throughout this contribution, visualization is carried out using *agrid* and *seaborn* (Waskom et al., 2020), both with underlying *matplotlib* (Hunter, 2007). We use perceptually linear color representations by SCM6 Crameri and Shephard (2019), as discussed by e.g., Morse et al. (2019) and Crameri et al. (2020).

3.1. Degree of Similarity

Previous studies, using the methodology that we develop in this contribution, used step functions within a given range to define similarity between observables (Goutorbe et al., 2011; Lucazeau, 2019). To take full advantage of our more limited selection of data, we refine this approach by using a smoothly decreasing function derived from the Gaussian distribution. By using this relation, the precise similarity range is more robust. The main drawback is the substantially increased computational cost. Degree of similarity between each reference observable and target observable is detected as:

$$S = \exp\left(-\frac{(o_R - o_T)^2}{2 \times (\sigma_R + \sigma_T)^2 / \Psi}\right), \tag{1}$$

where S is a degree of similarity in the range [0, 1]. o_R is the value of the reference observable, o_T is the value of the target observable, σ_R is the uncertainty (as two standard errors, 95.4%, range) for the reference observable, σ_T is the uncertainty for the target observable. Values used for σ are listed in Table 2. We introduce Ψ, a scalar representing similarity pickiness (Figure S10). A low value for Ψ relaxes the similarity function. We use the parameter to test and optimize the similarity detection (Figures 3 and S11). When an uncertainty range has been published with the datasets used as observables, we use this range. Shape index (Ebbing et al., 2018) is assigned a range of 1/8, as suggested by Koenderink and van Doorn (1992) to represent the categories of curvature shape. Classes are only accepted as similar when identical. This is achieved by using a very low value for σ. For most observables, the uncertainties are not defined. We optimize the similarity detection by performing a Monte Carlo simulation (N = 2,001) with random Ψ for each observable, and calculate cross-correlated misfit as MAe and RMSe, using the method described below. We find that the model is robust for defined ranges (Figures 3a and 3b, Figures S11 and S12). However, the acceptance range also functions as a spatial smoothing, as continuous data often change gradually. All acceptance ranges used are geologically and geophysical meaningful, and generally agree with our expected uncertainty in observables. Figure S12 provides the same test as Figures 3a and 3b, but also applying the step function similarity detection, to illustrate the less predictable response to parameter variations, for the limited range of observables used.

3.2. Weighting

A weight is introduced for sparse data and distance functions. A weighting of 1, sets the observable as fully relevant, but when the value decreases to 0, it is effectively muted from the similarity detection, and does not contribute to the heat flow estimate. The weights for heat production data are set to decrease linearly over 250 km from nearest observation (Figure S13). The impact of distance to volcanoes is set to decrease linearly over 100 km (Figure S14g). Beyond the maximum distance, the weighting is set to 0. Heat flow anomalies associated with advection and diffusion from shield volcanoes has a limited extent of less than 10 km (Hurwitz, 2003; Wright & Pilger, 2008). However, the existence of volcanoes also helps us to map the tectonic settings of volcanic provinces. The weighting functions are listed in Table 2. To assign dynamic weight, additional grids are constructed containing weighting factors. An example of the model with the distance to volcanoes observable excluded is provided by assigning a weight of zero (Figures S14a and S14b). We also generate a version without Moho and LAB observables (Figures S14c and S14d).

To investigate if an observable improves the result, or adds noise, we perform a Monte Carlo simulation with random weights assigned to the observables. We apply N = 2,001 random combinations, including the case with all observables weighted to 1. Keeping all observables fully weighted is demonstrated to provide good predictions (Figure S4).

10.1029/2020GC009428

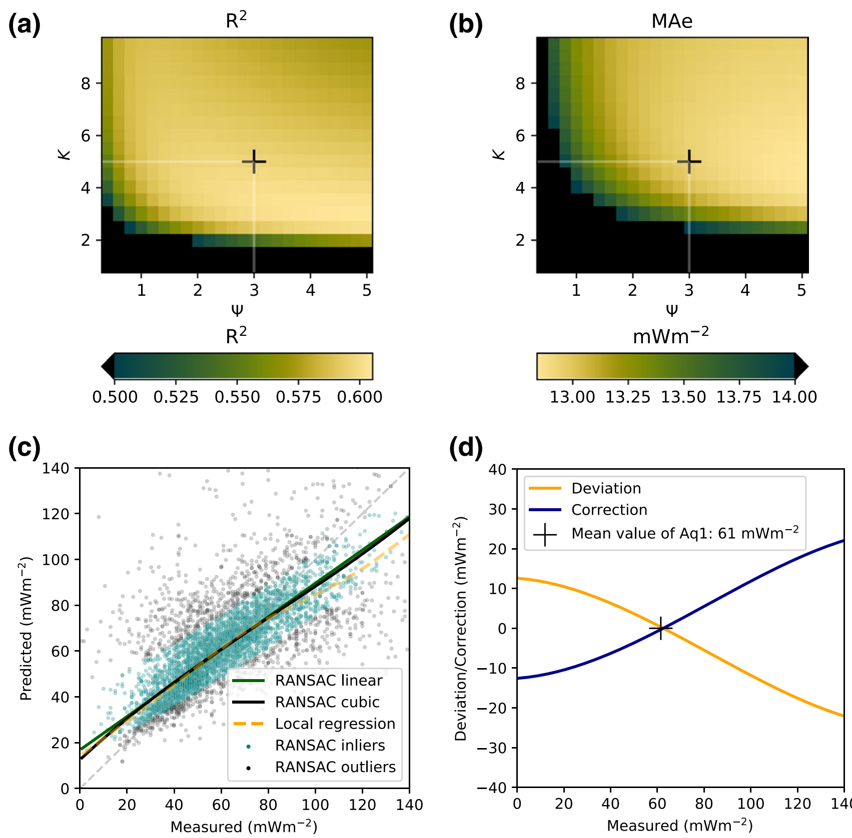

Figure 3. Method optimization and correction applied, using leave-one-out cross validation (LOOCV) of heat flow values in NGHF, included in this study. The R^2 value and MAe misfit cannot be optimized for the same parameter values. The choice of K and Ψ is therefore a trade-off between considerations, as discussed in text. (a) Parameter map for R^2. (b) Parameter map for Mean absolute error (MAe) misfit. K values at y-axis, and Ψ values at x-axis. Bright colors indicate more favorable combinations, the color range is optimized and values outside this range are masked black. (c) Heat flow measurements along the x-axis, and predicted values along y-axis. The RANSAC cubic regression (black line) gives a robust value, as outliers (gray dots) are ignored and the regression is estimated from inlier data points only (green dots) (Fischler & Bolles, 1981). A local regression (LOWESS) is shown with orange dashed line. A linear RANSAC regression line is also shown for reference (green line). (d) Applied correction to compensate variance reduction of heat flow records. Orange line shows the impact, and blue line shows the applied compensation. The black marker show the average heat flow in Aq1. LOWESS, locally weighted scatterplot smoothing.

3.3. Similarity Process and Optimization

For each Antarctic grid cell, observables are compared with reference observables' vectors for heat flow measurements to generate a similarity matrix. The similarities (S) are multiplied with the weighting matrix and stacked for each reference and target:

$$N_{sim} = \sum_{n_{obs}}^{i=1} S_{obs} \times w_{obs}, \tag{2}$$

where N_{sim} is the weighted similarity for each heat flow record, n_{obs} is the number of observables used (18), w_{obs} is the weighting for each observable for given heat flow record.

The stacked value N_{sim} is used as a power to a base K, to increase the value of multiple similar observables:

$$w_i = K^{N_{sim}} \tag{3}$$

To optimize and test the K parameter, together with the similarity pickiness (Ψ), we perform leave-one-out cross validation (LOOCV). We calculate misfit as root mean squared error (RMSe), mean absolute error (MAe), and coefficient of determination (R^2). The results are shown as a parameter maps in Figures 3a and 3b and Figure S12. MAe is reduced with higher K (Figure 3b), but the R^2 values (Figure 3a), and related RMSe (Figure S12a), suggests a lower value of K. With increasing Ψ, the spatial resolution increases (Figures S15d–S15f). K controls stability and accuracy. A high value of K would put more weight on fewer measurements, which reduces stability given the limited selection of observables available in Antarctica. In the lower range, $K < 3$, the resolution decreases and the output appears smoothed. High K and Ψ gives the best linear correlation, at the expense of increased RMSe and reduced R^2. We hence optimize for good RMSe within acceptable range of MAe, and then correct for the effects on correlation, selecting $K = 5$, and $\Psi = 3$. Maps resulting from different values of K and Ψ are provided in Figure S15. When comparing the parameter maps, we note that the continuous detection (Equation 1) provides a smoother, more robust and predictable response to variations in K and Ψ, for the selected parameter ranges (Figure S11).

3.4. Corrections of Heat Flow Values

A scatter plot of LOOCV predicted heat flow values and measurements shows that the overall trend captures the variations (Figure 3c). The residuals are heteroskedastic; high predicted values are underestimated. This is a result of extremely high values that cannot be detected due to rare combination of observables. We analyze the heteroskedasticity by fitting a local regression, a linear RANSAC regression, and a polynomial RANSAC regression (Fischler & Bolles, 1981). The local regression and the linear regressions are almost identical up to 80 mW m^{-2}. Above 80 mW m^{-2}, the local regression suggests an increasing underestimation of predicted values. Generally, predicted values are likely to gravitate toward the mean of the measurements as each predicted value is a weighted average of a large number of measurements and the selected similar distribution (σ_i) relates to the distribution of the total population as $\sigma_M = \sigma_i / \sqrt{w_i}$. When the K value is higher, fewer records get more of the weight, and smaller correction is needed. However, we show that the RMS error and coefficient of determination are better for moderate values of K, as the observables used in this study generate noise (Figure 3a). We accept the slightly skewed correlation, and apply a correction to account for the reduced range. We apply the RANSAC polynomial regressor to calculate a polynomial function for correction (Figure 3d):

$$Q_{\mathrm{pc}} = 2 \times Q_p - (a \times Q_p^3 + b \times Q_p^2 + c \times Q_p + d) \tag{4}$$

where Q_{pc} are the predicted and corrected heat flow values, Q_p are the predicted values. $a - d$ are the coefficients calculated for a cubic RANSAC regression using the Python package SKlearn (Pedregosa et al., 2011): $a = 13.72$, $b = -3.38$, $c = 0.9566$, $d = 0.01258$. The impact of the correction is shown in Figure S16, as maps and KDE plots of cross correlation.

3.5. Generating Maps of Heat Flow and Model Metrics

Using the optimized parameters, we calculate heat flow value and uncertainty metrics for each (x, y) target grid cell in Antarctica. Heat flow is calculated using:

$$\bar{Q} = \frac{\sum_i w_i q_i}{\sum_i w_i}, \tag{5}$$

where $\bar{Q}$ is the weighted mean of all heat flow measurements for the area represented by grid cell (x, y), q are the heat flow measurements from NGHF, and w_i is the weight from $w_i = K^{N_{sim}}$, where $K = 5$. Correction for reduced range is applied, as described in previous section.

The standard deviation of the heat flow values is used to calculate uncertainty:

$$\sigma_Q = \sqrt{\frac{\sum w_i (Q_i - \bar{Q})^2}{\sum w_i}}, \tag{6}$$

where σ_Q is the uncertainty assigned to the grid cell (Figure S17b). The uncertainties of the included heat flow records are not considered for this metric.

We also compute N_{total}, the amount of similarity from all observables and reference records, and present it as a logarithmic value. This is a combined measure of data availability, and how many similar reference observables are considered:

$$N_{\text{total}} = \ln \sum N_{sim}. \tag{7}$$

For each location, all weighted reference heat flow values are binned to a histogram, B_n, with bin size 1 mW m^{-2} in the range from 0 to 150 mW m^{-2}. The histogram is a discrete probability distribution and is normalized as:

$$p_A = \frac{B_n}{\sum B_n}. \tag{8}$$

Information entropy is calculated (Shannon, 1948):

$$H = -\sum_{n}^{i=1} p_A \ln p_A, \tag{9}$$

where $n = 150$, the number of bins, p_A is the normalized sum of similarity distribution (Equation 8). The base is e, and hence H is given in nats. The bins are also stored to an array, and histogram can be extracted for any location. The theoretical upper range of entropy for the used histogram is $\ln 150 = 5.01$.

Figure 4c shows entropy detected in each distribution of reference heat flow values. To facilitate interpretation of entropy in this context, Figure 4d shows six normalized histograms of similar geological settings and binned heat flow values. The background colors are identical with the colormap used in Figure 4c. The six distributions shown are chosen to divide the total range in five equal sized bins, exact locations are only provided for reference.

We generate grids for Antarctica in resolutions 20 × 20 km and 50 × 50 km (Figure S9). As a test case to appraise the approach and also to understand its limitations, we generate a heat flow grid of Australia in 20 × 20 km grid, GDA94/Australian Albers (epsg:3577) (Aq1.au, Figure S18). For the Australian test, we exclude heat production values to provide an estimate similar to the Antarctic conditions. For this map, we also exclude all Australian measurements from NGHF.

We calculate the differences between Aq1 and six previous heat flow maps, including Burton-Johnson et al. (2017) regional map of the Antarctic Peninsula. Grids are exported in interoperable formats as geoTIFF, netCDF and ascii tables using *agrid* functionality (Stål & Reading, 2020). We finally also generate a smoothed contour map by convolution with a Gaussian kernel with $\sigma = 40$ km (Figure 6).

4. Results

We present a new heat flow map for Antarctica, Aq1 (Figures 1 and 6, the latter labeled with geographic locations), together with maps of uncertainty metrics: standard deviation from the distribution of similar heat flow measurements in NGHF (Figure 4a), total number of similarities (Figure 4b), and the information entropy in the weighted heat flow histogram for each location (Figure 4c). Those maps inform the robustness of the assigned heat flow value.

For most of East Antarctica, we calculate a heat flow between 40 and 70 mW m^{-2}, which is a similar range to that found in previous studies (Figure 5). The lowest heat flow values are shown south of Dome Circle in interior Wilkes Land, Coats Land, and Wilkes Subglacial Basin. Elevated heat flow is shown in Victoria Land and parts of Queen Mary Land. High values of over 120 mW m^{-2} are shown in the Thwaites Glacier region, West Antarctica, and in Marie Byrd Land and Palmer Land. The map shows areas of moderate heat flow in parts of Siple Coast, Ellsworth Land, and central Antarctic Peninsula, down to 60 mW m^{-2}.

Compared with previous studies, Aq1 is similar to Shen et al. (2020), but shows higher heat flow in some West Antarctic volcanic provinces (Lough et al., 2013; van Wyk de Vries et al., 2018), and coastal East Antarctica (Figure 5e). Aq1 is generally lower in large parts of West Antarctica. In most regions, the differences between Aq1 and Shen et al. (2020) are within the uncertainty ranges. Compared to earlier Antarctic heat

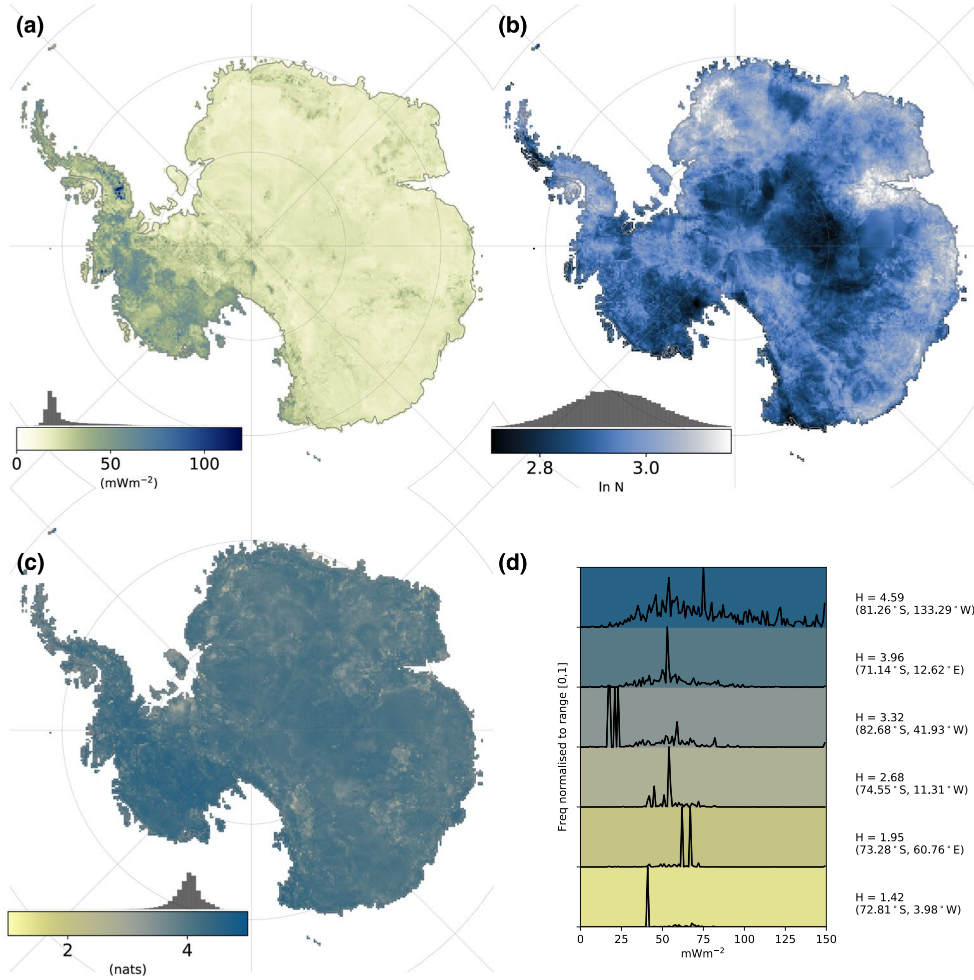

Figure 4. Uncertainty metrics for the Aq1 heat flow model. (a) Standard deviation of similar reference measurements. (b) Total number of similarities, in logarithmic scale. (c) Information entropy by natural logarithms, as described in methods section. (d) To assist the interpretation of information entropy, histograms from six examples are provided. The examples are the highest and lowest entropy, and four equal steps in between. The background color represent the same color as in (c). For clarity, the histograms of heat flow measurements are normalized to the range from 0 to 1. The color scales are chosen so that a darker tone indicates higher uncertainty, hence the scale for (b) is reversed.

flow models, Aq1 is most similar to An et al. (2015b), however with generally higher values in West Antarctica, and produced at higher resolution (Figure 5b). Aq1 also generally agrees with Martos et al. (2017) in East Antarctica, but assigns lower values in West Antarctic interior and the Antarctic Peninsula (Figure 5d). Aq1 is generally higher in East Antarctica than Fox Maule et al. (2005) (Figure 5a), but lower in Ellesworth Land, Oates Land and Mac. Robertson Land. We suggest high levels of heat flow in Palmer Land in the southern Antarctic Peninsula. This is in general agreement with earlier studies, particularly the regional study by Burton-Johnson et al. (2017) (Figure 5c). The pattern and range of the heat flow distribution in West Antarctica also agrees with O'Donnell et al. (2019), however, the multivariate approach provides higher spatial resolution. Finally, when Aq1 is compared with AqSS (Stål et al., 2020), the difference potentially points to areas with a neotectonic and volcanic contribution in West Antarctica: mainly Thwaites Glacier, Marie Byrd Land, and also coastal Victoria Land, and Queen Mary Land in East Antarctica (Figure 5f).

5. Discussion

In this section, we first note the limitations associated with the methodology. We then discuss how the alternative uncertainty metrics inform our appraisal and provide an interpretation of the Aq1 map.

10.1029/2020GC009428

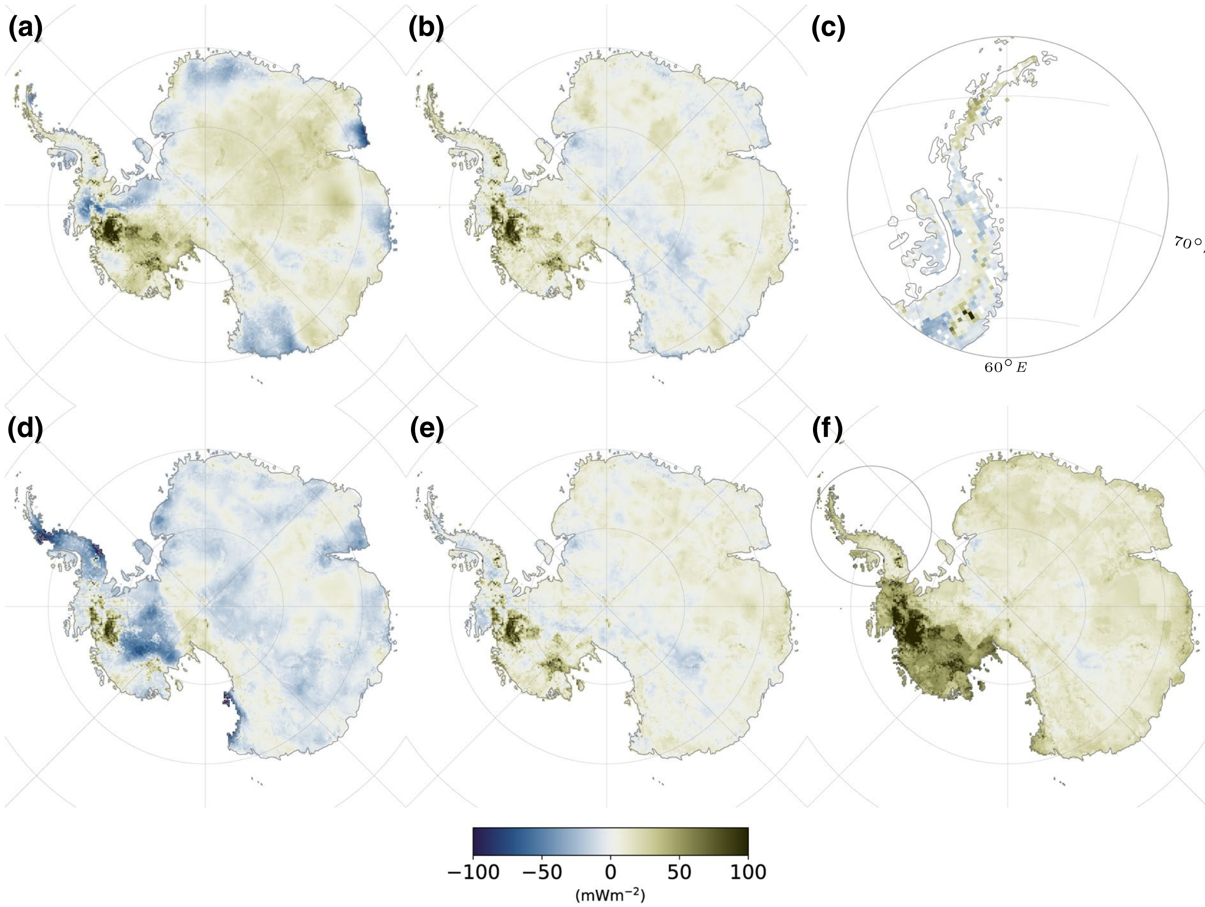

Figure 5. Comparison of Aq1 with previous published models. (a) Aq1—Fox Maule et al. (2005). (b) Aq1—An et al. (2015b). (c) Aq1—Burton-Johnson et al. (2017). (d) Aq1—Martos et al. (2017). (e) Aq1—Shen et al. (2020). (f) Aq1—AqSS (Stål et al., 2020). Outline of the Antarctic peninsula study (c) is shown in (f). Brown-green indicates that Aq1 shows higher heat flow values, the case for most of East Antarctica. Blue indicates that the model being compared shows higher heat flow. Average continental heat flow is near 65 mW m^{-2} (Pollack et al., 1993), Aq1 has a calculated average of 61.2 mW m^{-2}. The average for Fox Maule et al. (2005) is 63.1 mW m^{-2}, An et al. (2015b), 59.0 mW m^{-2}, Martos et al. (2017), p. 70.4 mW m^{-2}, and Shen et al. (2020), 57.1 mW m^{-2} (Figure S19), for the same extent as Aq1.

5.1. Limitations of the Similarity Approach

The similarity approach relies on the compatibility between reference and target observables, and we note that some matches are not ideal. As the best available choice of target observable, we use Antarctic datasets for Curie temperature depth (Martos et al., 2017), seismic Moho depth (An et al., 2015a), LAB (An et al., 2015b), and also a unique source for distance-to-nearest volcano (van Wyk de Vries et al., 2018). The matches between the reference and target observables across Antarctica (Figure S6) show significant differences. While the impact of those differences is difficult to quantify, we provide robust maps of uncertainty metrics for the resulting model. The incompatibility between reference and target observables is a potential explanation for large uncertainties and information entropy (Figure 4), where global and regional datasets associate different tectonic settings. The impact of uncertainties and shortcomings of the datasets used is moderated by using multiple sets of observables.

The leave-one-out cross-validation Monte Carlo tests (Figure S4) show that each used observable improves the prediction, even as some of the datasets are usually not associated with thermal properties. Instead, they support tectonic association. The MAe misfit is around 12 mW m^{-2}, which is encouraging (Figure 3b). We note, however, that heat flow datasets are affected by sample bias, particularly in Antarctica's Gondwanan neighbors. Heat flow measurements are often targeted on regions with particular economic interest, and might not well represent the average Antarctic continent. Records from mountainous areas are likely to be mostly from valleys rather than ridges, and hence higher heat flow due to topographic focusing (e.g.,

10.1029/2020GC009428

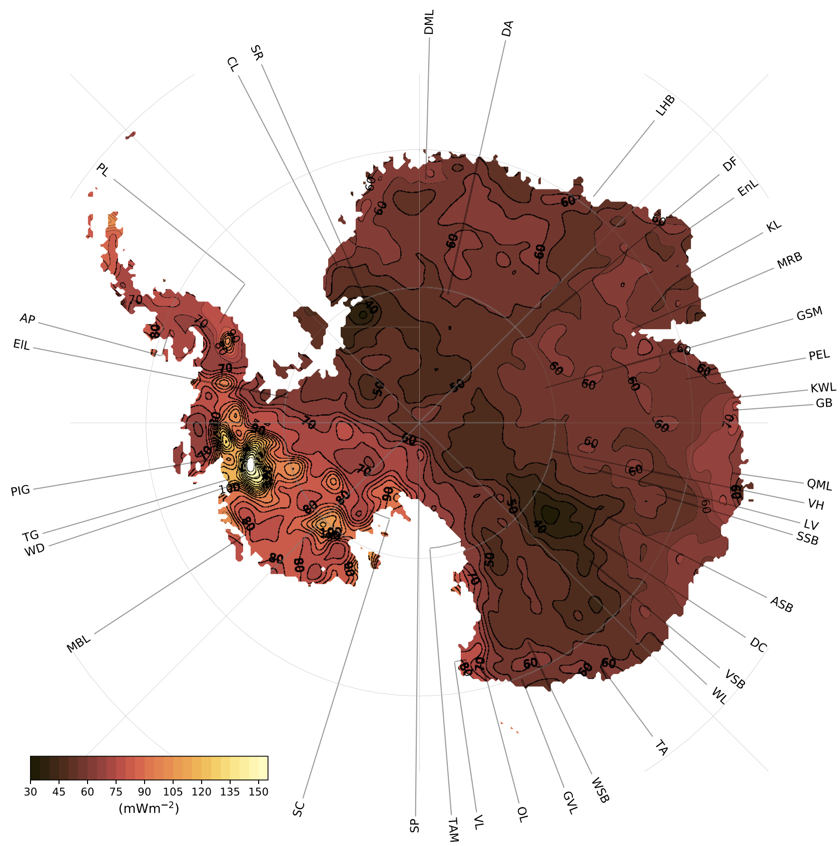

Figure 6. Locations mentioned in text, and an alternative visualization of Aq1. Heat flow is shown as smoothed contours to enable reading of numerical values, although some detail is lost. Smoothing is carried out using a Gaussian kernel with $\sigma = 40$ km. Geographic locations mentioned in text: AP, Antarctic Peninsula; ASB, Aurora Subglacial Basin; CL, Coats Land; DA, Dome Argus; DC, Dome Circle; DF, Dome Fuji; DML, Dronning Maud Land; EIL, Ellsworth Land; EnL, Enderby Land; GB, Gaussberg; GSM, Gamburtsev Subglacial Mountains; GVL, George V Land; KL, Kemp Land; KWL, Kaiser Wilhelm II Land; LHB, Lützow-Holm Bay; LV, Lake Vostok; MBL, Marie Byrd Land; MRB, Mac. Robertson Land; OL, Oates Land; PEL, Princess Elizabeth Land; PIG, Pine Island Glacier; PL, Palmer Land; QML, Queen Mary Land; SC, Siple Coast; SP, South Pole; SSB, Shmidt Subglacial Basin; SR, Shackleton Range; TA, Terre Adélie; TAM, Transantarctic Mountains; TG, Thwaites Glacier; VH, Vostok Highlands; VL, Victoria Land; VSB, Vincennes Subglacial Basin; WD, West Antarctic Ice Sheet (WAIS) divide; WL, Wilkes Land; WSB, Wilkes Subglacial Basin.

Beardsmore & Cull, 2001; Lees, 1910). Heat production and heat flow can vary over a large range in a short distance (Figure S13). We therefore keep all individual records instead of cell or kernel averages. This might further skew the reference heat flow distribution.

5.2. Methodology Appraisal

We test the methodology using the example of the Australian continent, and achieve a generally good prediction (Figure S18). However, a few locations show values where the calculated value is far too low. The most striking misfits are generally associated with areas known for high crustal heat production (Figure S18b) (e.g., Holgate et al., 2010; McLaren et al., 2003), and those measurements are indeed targeted on geothermal energy or mineral exploration with an interest in enriched radioactive elements. The Australian example suggest that our method captures important properties of the crust, but observables used might fail to assign an extreme value associated with shallow high heat production. The resulting ambiguity with observables used, manifests as increasing noise, uncertainty and information entropy. The cross correlation suggests agreement with the parameter choices made in previous studies (Goutorbe et al., 2011; Lucazeau, 2019), but high value of K and Ψ create an overfitted prediction with the observables used. We aim to avoid overfitting by choosing parameters in a range with low sensitivity for parameter values (Figures 3a and 3b).

10.1029/2020GC009428

Heat flow measurements in NGHF, we assume, do not represent all tectonic settings equally. By using the exponential function controlled by the *K* parameter, however, only a few measurements will define the heat flow distribution from similar locations. The results depend on the accuracy resulting from the combination of observables used, and the quality and selection of heat flow records. Using different subsets of heat flow values can modify the resulting map, e.g., without the distance to volcano observable (Figures S14a and S14b), without the Moho depth and LAB depth observables (Figures S14c and S14d), and excluding all measurements deeper than 250 m, which yields lower calculated values in the Thwaites region (Figures S14e and S14f).

5.3. Discussion of Uncertainties

We aim to communicate the uncertainties inherent in Aq1 in a way that is informative of the different mechanisms through which uncertainty arises. For example, mapped uncertainty measures often fail to contain the progression of uncertainty from assumptions (e.g., Pérez-Díaz et al., 2020). Our first uncertainty metric is the standard deviation of reference heat flow records weighted with similarly (Figure 4a). This distribution does not account for the total range of choices made when including observables, acceptance ranges for similarity and weighting, or absent observables as heat production and sediment cover. Therefore, we also provide maps of total number of similarities, and information entropy (Shannon, 1948). The number of similarities map (Figure 4b), indicates how well the tectonic setting is represented in the heat flow catalog, and how much data are available in Antarctica. In this map, e.g., the Gamburtsev Subglacial Mountains stand out as a region with few similarities elsewhere. Figure 4c shows how much information is captured by the similarity process. A few areas, such as the northern Antarctic Peninsula, Ellsworth Land and west of Miller Range are shown to be very robust in our model. We believe that the inclusion of information entropy as a proxy for uncertainty is a useful tool in geophysical and geological studies, particularly in multivariate and multidimensional models (e.g., Wellmann & Regenauer-Lieb, 2012). In our map, the information entropy metric also captures multi modal distributions, and a low entropy value can enable the reduction of apparently large uncertainty to a few discrete possibilities.

5.4. Interpretation

Aq1 improves the information available to the geological community by supplying a heat flow map that is of higher resolution than previous studies. The exact resolution is difficult to quantify, as each observable contributes different levels of detail. The resolution of the datasets used in previous studies (An et al., 2015b; Martos et al., 2017) is improved upon somewhat, in Aq1, through the addition of constraints from the higher resolution elevation model and airborne Bouguer anomalies. It also provides a quantified means of incorporating information through the match between reference and target observables that inform the contribution to heat flow from the probable subglacial geology. Aq1 agrees with previous studies in suggesting generally higher heat flow in West Antarctica, and lower in East Antarctica. This is also in accordance with our understanding of the tectonic development of the continent (e.g., Artemieva & Thybo, 2020; Boger, 2011; Harley et al., 2013; Jordan et al., 2020), and large-scale geophysics (e.g., Haeger et al., 2019). Our map adds detail to this relationship by suggesting a few pronounced hot spots in East Antarctica, and also areas with moderate heat flow in parts of West Antarctica (Figure 6). The highest values are computed for the interior of Thwaites Glacier and Pine Island Glacier. The region is categorized by thin crust (e.g., Damiani et al., 2014), steep geothermal gradient (e.g., O'Donnell et al., 2019), and a complex tectonic setting that is under current discussion (Artemieva & Thybo, 2020; Ferraccioli et al., 2007; Jordan et al., 2020). Our values are locally higher than previous continental scale heat flow studies (Figure 5), and in accordance with observations from radar sounding of the ice-bedrock interface (Schroeder et al., 2014) and field measurements (e.g., Clow et al., 2014), however, the uncertainties remain large. Aside from Thwaites Glacier region, the Aq1 model does not show any extended regions of heat flow over 100 mW m^{-2} (Figures S20d).

We note that Aq1 is most similar to Shen et al. (2020), and we take this similarity as a strong evidence to support the validity of both 2020 studies, as they are effectively independent studies. Shen et al. (2020) is not derived from the datasets used for Aq1, and a different methodology is used. In particular, there is a convincing similarity between the two models in the overall pattern in West Antarctica (Figure 5e), however Aq1 assigns higher values in the Thwaites region and northern Siple Coast (Figure 5e).

10.1029/2020GC009428

Elevated heat, over 70 mW m^{-2}, is detected in East Antarctica, for example, in interior Queen Mary Land, near the Gaussberg Volcano (Figure 6). Due to the lack of geophysical data, the Gaussberg volcano is still poorly understood, but its recent volcanism has potential clues to the heat flow of an extended region. However, we note that even if distance to volcanoes observable is excluded (Figure S14a and 14b), the model still renders an elevated heat flow in the Gaussberg region. The low heat flow values from the Wilkes Subglacial Basin and inland from Wilkes Land, and to some extent Aurora Subglacial Basin and Vincennes Subglacial Basin might be a result of sediments with low thermal conductivity (Jessop & Majorowicz, 1994), or low heat production in underlying cratonic crystalline basement (Stål et al., 2020).

Aq1 suggests a relatively moderate heat flow in central Siple Coast. Values based on direct measurements in the region gives a large range of heat flow values. This variance is likely caused by a number of local subglacial processes such as hydrothermal circulation and potentially volcanism with a very large impact the measured heat (Begeman et al., 2017; Engelhardt, 2004; Siegert et al., 2016; Tulaczyk et al., 2001). Such high values are not captured at this scale given the resolution of the available observables, and we don't expect to see extremely high values when averaged over a 400 km^2 grid cell. Sedimentary basins might also hamper the heat flow due to the lower thermal conductivity and groundwater circulation (Jessop & Majorowicz, 1994).

Due to the low number of heat flow measurements in Antarctica, the high variability of heat flow, and the assumptions involved (discussed by e.g., Burton-Johnson et al., 2020; Mony et al., 2020), we suggest that a direct comparison is not meaningful for a continental scale map. However, Aq1 still agrees well with the existing measurements compiled by Burton-Johnson et al. (2020) (Figure S21).

5.5. Future Directions

The Aq1 model, released as the central product in this contribution, is a suitable input to ice sheet models and other interdisciplinary studies of interacting Earth systems in Antarctica. However, some parts of the model show large uncertainties that should be reduced in future work. Additional datasets and data products for possible inclusion in updates include those from recent seismic studies (Lloyd et al., 2020; Shen et al., 2018). With additional magnetic data, further derivatives could be included to assist in higher resolution tectonic association, as has been achieved in regional studies (e.g., Ferraccioli et al., 2001; Goodge & Finn, 2010; Ruppel et al., 2018).

Comparison with heat flow models based on solid Earth data potentially provide further constraints on the nature of the subglacial environment. Additional constraints from observed geology, and thickness and nature of subglacial sediments are further datasets of potential utility that could be included in a probabilistic framework, in the absence of well-distributed direct observations. For the next generation of Antarctic heat flow models, it may be appropriate to include data from the ice sheet community in a truly interdisciplinary initiative. The existence of subglacial melt, hydrological information, and insights from the dynamics of the ice sheet are candidate datasets for inclusion.

For some regions, the model could be refined with a topographic correction (e.g., Beardsmore & Cull, 2001; Lees, 1910), which would require additional consideration for interpolation of the roughness of subglacial topography data (Graham et al., 2017). Related to considerations of topography, the exhumation and erosion history of Antarctica has a considerable impact on subglacial heat flow and merits inclusion in future work. Our understanding of such processes has developed over the past decade (e.g., Paxman et al., 2019; Tooze et al., 2020; Wilson et al., 2012). A recent marine seismic interpretation (Sauermilch et al., 2019) shows large volumes of offshore sediments. Considering those results may enable better constrained models of regional erosion and exhumation, with further impact on heat flow.

We hope that Aq1 will be used to provide clues on subglacial tectonic settings, and also used by the interdisciplinary community working on interactions and feedbacks of the cryosphere and solid-Earth systems. We anticipate that ice sheet evolution models will continue to be refined in response to updated heat flow maps. Adopting updatable models, such as Aq1, will readily enable the improvement of results that make use of heat flow as a model input.

6. Conclusion

The new geothermal heat flow model, Aq1, is based on a new approach to the estimation of subglacial heat flow for Antarctica. We use a multivariate analysis, modified to take account of the strengths and limitations of currently available geophysical and geological datasets for Antarctica. This analysis complements the univariate techniques that underpin alternative heat flow maps for the continent. The resulting maps depend on a robust number of observables and enable constraints to be included from comparative records of heat flow and tectonic setting, elsewhere in the world. The Aq1 model is supplied together with an open computational framework to facilitate future refinements as new datasets become available. In agreement with models constrained by univariate approaches, Aq1 shows elevated heat flow in West Antarctica, low heat flow values in East Antarctica, and refined heat flow estimates throughout. Highest values are shown in Thwaites Glacier. Moderate heat flow is suggested for Siple Coast and Ellsworth Land, West Antarctica. Elevated heat values are modeled for some areas of East Antarctica, for example, the region near Gaussberg in Kaiser Wilhelm II Land, Queen Mary Land, and northern Victoria Land. Aq1 provides higher resolution compared with previous models, and robust uncertainty metrics.

Data Availability Statement

The Aq1 model is available in interoperable formats (geoTIFF, netCDF, and comma-separated values (CSV) text file) in 20 and 50 km resolution grids from PANGAEA data library (https://doi.org/10.1594/PANGAEA.924857) (Stål et al., 2020). Python code used to generate the maps in this study is available from online repositories (latest version at https://github.com/TobbeTripitaka/Aq1, archived at https://zenodo.org/record/4014430). Details regarding data and code download are provided with the Supporting Information. The software and data framework is described in detail by Stål and Reading (2020) and Stål et al. (2020).

Acknowledgments
This research is a contribution to the SCAR SERCE program. We are grateful to Rebecca Carey, Felicity McCormack, Steven Phipps and Ross Turner for valuable discussions and feedback. We also wish to thank the two anonymous reviewers, that substantially contributed to this study. This research was supported under Australian Research Council's Special Research Initiative for Antarctic Gateway Partnership (Project ID SR140300001). The authors declare that they have no conflict of interest.

References

Afonso, J. C., Salajegheh, F., Szwillus, W., Ebbing, J., & Gaina, C. (2019). A global reference model of the lithosphere and upper mantle from joint inversion and analysis of multiple data sets. *Geophysical Journal International*, *217*(3), 1602–1628. https://doi.org/10.1093/gji/ggz094

Aitken, A. R., Young, D. A., Ferraccioli, F., Betts, P. G., Greenbaum, J. S., Richter, T. G., et al. (2014). The subglacial geology of Wilkes Land, East Antarctica. *Geophysical Research Letters*, *41*, 2390–2400. https://doi.org/10.1002/2014GL059405

Amante, C., & Eakins, B. (2009). ETOPO1 1 arc-minute global relief model (*NOAA Tech. Memo. NESDIS NGDC-24*, 19 pp.). Boulder, CO: National Geophysical Data Center Marine Geology and Geophysics Division.

An, M., Wiens, D. A., Zhao, Y., Feng, M., Nyblade, A. A., Kanao, M., et al. (2015a). S-velocity model and inferred Moho topography beneath the Antarctic Plate from Rayleigh waves. *Journal of Geophysical Research: Solid Earth*, *120*, 359–383. https://doi.org/10.1002/2014JB011332

An, M., Wiens, D. A., Zhao, Y., Feng, M., Nyblade, A., Kanao, M., et al. (2015b). Temperature, lithosphere-asthenosphere boundary, and heat flux beneath the Antarctic Plate inferred from seismic velocities. *Journal of Geophysical Research: Solid Earth*, *120*, 8720–8742. https://doi.org/10.1002/2015JB011917

Artemieva, I. M. (2011). *The Lithosphere: An interdisciplinary approach*. Cambridge, UK: Cambridge University Press.

Artemieva, I. M., & Mooney, W. D. (2001). Thermal thickness and evolution of Precambrian lithosphere: A global study. *Journal of Geophysical Research: Solid Earth*, *106*(B8), 16387–16414. https://doi.org/10.1029/2000jb900439

Artemieva, I. M., & Thybo, H. (2020). Continent size revisited: Geophysical evidence for West Antarctica as a back-arc system. *Earth-Science Reviews*, *202*, 103106. https://doi.org/10.1016/j.earscirev.2020.103106

Beardsmore, G. R., & Cull, J. P. (2001). *Crustal heat flow*. Cambridge, UK: Cambridge University Press. https://doi.org/10.1017/cbo9780511606021

Becker, T. W., & Boschi, L. (2002). A comparison of tomographic and geodynamic mantle models. *Geochemistry, Geophysics, Geosystems*, *3*, 1003. https://doi.org/10.1029/2001GC000168

Begeman, C. B., Tulaczyk, S. M., & Fisher, A. T. (2017). Spatially variable geothermal heat flux in West Antarctica: Evidence and implications. *Geophysical Research Letters*, *44*, 9823–9832. https://doi.org/10.1002/2017GL075579

Bentley, J. L. (1975). Multidimensional binary search trees used for associative searching. *Communications of the ACM*, *18*(9), 509–517. https://doi.org/10.1145/361002.361007

Boger, S. D. (2011). Antarctica—Before and after Gondwana. *Gondwana Research*, *19*(2), 335–371. https://doi.org/10.1016/j.gr.2010.09.003

Burton-Johnson, A., Black, M., Peter, T. F., & Kaluza-Gilbert, J. (2016). An automated methodology for differentiating rock from snow, clouds and sea in Antarctica from Landsat 8 imagery: A new rock outcrop map and area estimation for the entire Antarctic continent. *The Cryosphere*, *10*(4), 1665–1677. https://doi.org/10.5194/tc-10-1665-2016

Burton-Johnson, A., Dziadek, R., & Martin, C. (2020). Geothermal heat flow in Antarctica: Current and future directions. *The Cryosphere Discussions*, 1–45. https://doi.org/10.5194/tc-2020-59

Burton-Johnson, A., Halpin, J. A., Whittaker, J. M., Graham, F. S., & Watson, S. J. (2017). A new heat flux model for the Antarctic Peninsula incorporating spatially variable upper crustal radiogenic heat production. *Geophysical Research Letters*, *44*, 5436–5446. https://doi.org/10.1002/2017GL073596

Carson, C. J., McLaren, S., Roberts, J. L., Boger, S. D., & Blankenship, D. D. (2014). Hot rocks in a cold place: High sub-glacial heat flow in East Antarctica. *Journal of the Geological Society*, *171*(1), 9–12. https://doi.org/10.1144/jgs2013-030

Cleveland, W. S. (1979). Robust locally weighted regression and smoothing scatterplots. *Journal of the American Statistical Association*, *74*(368), 829–836. https://doi.org/10.1080/01621459.1979.10481038

Clow, G. D., Cuffey, K., & Waddington, E. (2014). High heat-flow beneath the central portion of the west Antarctic ice sheet. (1, pp. C31A–C0577). Washington, DC: American Geophysical Union.

Crameri, F., & Shephard, G. E. (2019). Scientific color maps. *Zenodo*. https://doi.org/10.5281/zenodo.3596401

Crameri, F., Shephard, G. E., & Heron, P. J. (2020). The misuse of color in science communication. *Nature Communications*, *11*, 5444. https://doi.org/10.1038/s41467-020-19160-7

Damiani, T. M., Jordan, T. A., Ferraccioli, F., Young, D. A., & Blankenship, D. D. (2014). Variable crustal thickness beneath Thwaites Glacier revealed from airborne gravimetry, possible implications for geothermal heat flux in West Antarctica. *Earth and Planetary Science Letters*, *407*, 109–122.doi https://doi.org/10.1016/j.epsl.2014.09.023

DeConto, R. M., & Pollard, D. (2016). Contribution of Antarctica to past and future sea-level rise. *Nature*, *531*(7596), 591–597. https://doi.org/10.1038/nature17145

Drewes, H., Kuglitsch, F., Adám, J., & Rózsa, S. (2016). The geodesists handbook 2016. *Journal of Geodesy*, *90*(10), 907–1205. https://doi.org/10.1007/s00190-016-0948-z

Dziadek, R., Gohl, K., Diehl, A., & Kaul, N. (2017). Geothermal heat flux in the Amundsen Sea sector of West Antarctica: New insights from temperature measurements, depth to the bottom of the magnetic source estimation, and thermal modeling. *Geochemistry Geophysics Geosystems*, *18*, 2657–2672. https://doi.org/10.1002/2016GC006755

Ebbing, J., Haas, P., Ferraccioli, F., Pappa, F., Szwillus, W., & Bouman, J. (2018). Earth tectonics as seen by GOCE—Enhanced satellite gravity gradient imaging. *Scientific Reports*, *8*(1), 1–9. https://doi.org/10.1038/s41598-018-34733-9

Engelhardt, H.. (2004). Thermal regime and dynamics of the West Antarctic ice sheet. *Annals of Glaciology*, *39*, 85–92. https://doi.org/10.3189/172756404781814203

England, P. C., & Richardson, S. W. (1980). Erosion and the age dependence of continental heat flow. *Geophysical Journal of the Royal Astronomical Society*, *62*(2), 421–438. https://doi.org/10.1111/j.1365-246X.1980.tb04865.x

Ferraccioli, F., Coren, F., Bozzo, E., Zanolla, C., Gandolfi, S., Tabacco, I., & Frezzotti, M. (2001). Rifted(?) crust at the East Antarctic Craton margin: Gravity and magnetic interpretation along a traverse across the Wilkes Subglacial Basin region. *Earth and Planetary Science Letters*, *192*(3), 407–421. https://doi.org/10.1016/S0012-821X(01)00459-9

Ferraccioli, F., Jordan, T. A., Vaughan, D. G., Holt, J., James, M., Corr, H., et al. (2007). New aerogeophysical survey targets the extent of the West Antarctic Rift System over Ellsworth Land, in Antarctica. In A. K. Cooper, & C. R. Raymond (Eds.), *A keystone in a changing world online proceedings of the 10th International Symposium on Antarctic Earth Sciences (USGS of-2007-1047,* (pp. 2004–2007).Washington, DC: U.S. Geological Survey and The National Academies.

Fischler, M. A., & Bolles, R. C.. (1981). Random sample consensus: A paradigm for model fitting with applications to image analysis and automated cartography. *Communications of the ACM*, *24*(6), 381–395. https://doi.org/10.1145/358669.358692

Fisher, A. T., Mankoff, K. D., Tulaczyk, S. M., Tyler, S. W., & Foley, N. (2015). High geothermal heat flux measured below the West Antarctic Ice Sheet. *Science Advances*, *1*(6), 1–9. https://doi.org/10.1126/sciadv.1500093

Förste, C., Bruinsma, S., Flechtner, F., Marty, J.-C., Dahle, C., Abrykosov, O., et al. (2013). EIGEN-6C2-A new combined global gravity field model including GOCE data up to degree and order 1949 of GFZ Potsdam and GRGS Toulouse. EGU general assembly conference abstracts (15, p. 4077). Vienna: EGU Services, G.F.Z. Data.

Fox Maule, C., Purucker, M. E., Olsen, N., & Mosegaard, K. (2005). Geophysics: Heat flux anomalies in Antarctica revealed by satellite magnetic data. *Science*, *309*(5733), 464–467. https://doi.org/10.1126/science.1106888

Fretwell, P., Pritchard, H. D., Vaughan, D. G., Bamber, J. L., Barrand, N. E., Bell, R., et al. (2012). Bedmap2: Improved ice bed, surface and thickness datasets for Antarctica. *The Cryosphere Discussions*, *6*(5), 4305–4361. https://doi.org/10.5194/tcd-6-4305-2012

Fudge, T. J., Steig, E. J., Markle, B. R., Schoenemann, S. W., Ding, Q., Taylor, K. C., et al. (2013). Onset of deglacial warming in West Antarctica driven by local orbital forcing. *Nature*, *500*(7463), 440–444. https://doi.org/10.1038/nature12376

Gard, M., Hasterok, D., & Halpin, J. A. (2019). Global whole-rock geochemical database compilation. *Earth System Science Data*, *11*(4), 1553–1566. https://doi.org/10.5194/essd-11-1553-2019

Global Volcanism Program. (2013). *Volcanoes of the World, v. 4.9.0*. Venzke, E. (ed.). Washington, DC: Smithsonian Institution. https://doi.org/10.5479/si.GVP.VOTW4-2013

Golledge, N. R., Kowalewski, D. E., Naish, T. R., Levy, R. H., Fogwill, C. J., & Gasson, E. G. W. (2015). The multi-millennial Antarctic commitment to future sea-level rise. *Nature*, *526*(7573), 421–425. https://doi.org/10.1038/nature15706

Golynsky, A. V., Ferraccioli, F., Hong, J. K., Golynsky, D. A., von Frese, R. R., Young, D. A., et al. (2018). New magnetic anomaly map of the Antarctic. *Geophysical Research Letters*, *45*, 6437–6449. https://doi.org/10.1029/2018GL078153

Goodge, J. W. (2018). Crustal heat production and estimate of terrestrial heat flow in central East Antarctica, with implications for thermal input to the East Antarctic ice sheet. *The Cryosphere*, *12*(2), 491–504. https://doi.org/10.5194/tc-12-491-2018

Goodge, J. W., & Finn, C. A. (2010). Glimpses of East Antarctica: Aeromagnetic and satellite magnetic view from the central transantarctic mountains of East Antarctica. *Journal of Geophysical Research*, *115*, B09103. https://doi.org/10.1029/2009JB006890

Goutorbe, B., Poort, J., Lucazeau, F., & Raillard, S. (2011). Global heat flow trends resolved from multiple geological and geophysical proxies. *Geophysical Journal International*, *187*(3), 1405–1419. https://doi.org/10.1111/j.1365-246X.2011.05228.x

Graham, F. S., Roberts, J. L., Galton-Fenzi, B. K., Young, D., Blankenship, D., & Siegert, M. J. (2017). A high-resolution synthetic bed elevation grid of the Antarctic continent. *Earth System Science Data*, *9*(1), 267–279. https://doi.org/10.5194/essd-9-267-2017

Griggs, J. A., & Bamber, J. L. (2011). Antarctic ice-shelf thickness from satellite radar altimetry. *Journal of Glaciology*, *57*(203), 485–498. https://doi.org/10.3189/002214311796905659

Grosse, P., Euillades, P. A., Euillades, L. D., & van Wyk de Vries, B.. (2014). A global database of composite volcano morphometry. *Bulletin of Volcanology*, *76*(1), 784. https://doi.org/10.1007/s00445-013-0784-4

Haeger, C., Kaban, M. K., Tesauro, M., Petrunin, A. G., & Mooney, W. D. (2019). 3-D density, thermal, and compositional model of the Antarctic lithosphere and implications for its evolution. *Geochemistry Geophysics Geosystems*, *20*, 688–707. https://doi.org/10.1029/2018GC008033

Harley, S. L., Fitzsimons, I. C., & Zhao, Y. (2013). Antarctica and supercontinent evolution: Historical perspectives, recent advances and unresolved issues. *Geological Society Special Publication*, *383*(1), 1–34. https://doi.org/10.1144/SP383.9

Harris, C. R., Millman, K. J., van der Walt, S. J., Gommers, R., Virtanen, P., Cournapeau, D., et al. (2020). Array programming with NumPy. *Nature*, *585*(7825), 357–362. https://doi.org/10.1038/s41586-020-2649-2

Hartmann, J., & Moosdorf, N. (2012). The new global lithological map database GLiM: A representation of rock properties at the Earth surface. *Geochemistry, Geophysics, Geosystems*, *13*, Q12004. https://doi.org/10.1029/2012GC004370

Hasterok, D. (2019). *Thermoglobe*. Retrieved from www.heatflow.org

Hasterok, D., & Chapman, D. S. (2011). Heat production and geotherms for the continental lithosphere. *Earth and Planetary Science Letters*, *307*(1–2), 59–70. https://doi.org/10.1016/j.epsl.2011.04.034

Hasterok, D., Gard, M., & Webb, J. (2018). On the radiogenic heat production of metamorphic, igneous, and sedimentary rocks. *Geoscience Frontiers*, *9*(6), 1777–1794. https://doi.org/10.1016/j.gsf.2017.10.012

Hasterok, D., & Webb, J. (2017). On the radiogenic heat production of igneous rocks. *Geoscience Frontiers*, *8*(5), 919–940. https://doi.org/10.1016/j.gsf.2017.03.006

Holgate, F. L., Goh, H. K. H., Wheller, G., & Lewis, R. G. J. (2010). The Central Tasmanian geothermal anomaly: A prospective new EGS province in Australia. In *World geothermal congress 2010* (pp. 25–29). Bali, Indonesia. Retrieved from https://pangea.stanford.edu/ERE/db/IGAstandard/record_detail.php?id=6681

Hunter, J. D. (2007). Matplotlib: A 2D graphics environment. *Computing in Science & Engineering*, *9*(3), 99–104. https://doi.org/10.1109/MCSE.2007.55

Hurwitz, S.. (2003). Groundwater flow, heat transport, and water table position within volcanic edifices: Implications for volcanic processes in the Cascade Range. *Journal of Geophysical Research*, *108*(B12), 2557. https://doi.org/10.1029/2003JB002565

Jaupart, C., & Mareschal, J. C. (2014). 4.2 – Constraints on Crustal Heat Production from Heat Flow Data In H. D. Holland & K. K. Turekian (Eds.), *Treatise on Geochemistry* (2nd ed., pp. 53–73). Oxford: Elsevier. https://doi.org/10.1016/B978-0-08-095975-7.00302-8

Jaupart, C., Mareschal, J. C., & Iarotsky, L. (2016). Radiogenic heat production in the continental crust. *Lithos*, *262*, 398–427. https://doi.org/10.1016/j.lithos.2016.07.017

Jessop, A. M., & Majorowicz, J. A. (1994). Fluid flow and heat transfer in sedimentary basins. *Geological Society Special Publication*, *78*(78), 43–54. https://doi.org/10.1144/GSL.SP.1994.078.01.05

Jones, E., Oliphant, T., Peterson, P., & Others. (2015). *SciPy: Open source Scientific tools for Python, 2001*. Retrieved from http://www.scipy.org/

Jordan, T. A., Riley, T. R., & Siddoway, C. S. (2020). The geological history and evolution of West Antarctica. *Nature Reviews Earth & Environment*, *1*(2), 117–133. https://doi.org/10.1038/s43017-019-0013-6

Koenderink, J. J., & van Doorn, A. J. (1992). Surface shape and curvature scales. *Image and Vision Computing*, *10*(8), 557–564. https://doi.org/10.1016/0262-8856(92)90076-F

Larour, E., Morlighem, M.., Seroussi, H., Schiermeier, J., & Rignot, E.. (2012). Ice flow sensitivity to geothermal heat flux of Pine Island Glacier, Antarctica. *Journal of Geophysical Research*, *117*, F04023. https://doi.org/10.1029/2012JF002371

Laske, G., Masters, G., Ma, Z., & Pasyanos, M. (2013). Update on CRUST1.0—A 1-degree global model of Earth's crust. In *EGU general assembly 2013* (Vol. *15*, p. 2658). Retrieved from http://meetingorganizer.copernicus.org/EGU2013/EGU2013-2658.pdf

Lees, C. H. (1910). On the shapes of the isogeotherms under mountain ranges in radio-active districts. *Proceedings of the Royal Society of London Series A: Containing Papers of a Mathematical and Physical Character*, *83*(563), 339–346. https://doi.org/10.1098/rspa.1910.0022

Levy, F., Jaupart, C., Mareschal, J. C., Bienfait, G., & Limare, A. (2010). Low heat flux and large variations of lithospheric thickness in the Canadian Shield. *Journal of Geophysical Research*, *115*, B06404. https://doi.org/10.1029/2009JB006470

Li, C. F., Lu, Y., & Wang, J. (2017). A global reference model of Curie-point depths based on EMAG2. *Scientific Reports*, *7*, 45129. https://doi.org/10.1038/srep45129

Lloyd, A. J., Wiens, D. A., Zhu, H., Tromp, J., Nyblade, A. A., Aster, R. C., et al. (2020). Seismic structure of the Antarctic upper mantle imaged with adjoint tomography. *Journal of Geophysical Research: Solid Earth*, *125*, 2019JB017823. https://doi.org/10.1029/2019JB017823

Lösing, M., Ebbing, J., & Szwillus, W. (2020). Geothermal heat flux in Antarctica: Assessing models and observations by Bayesian inversion. *Frontiers of Earth Science*, *8*, 105. https://doi.org/10.3389/feart.2020.00105

Lough, A. C., Wiens, D. A., Grace Barcheck, C., Anandakrishnan, S., Aster, R. C., Blankenship, D. D., et al. (2013). Seismic detection of an active subglacial magmatic complex in Marie Byrd Land, Antarctica. *Nature Geoscience*, *6*(12), 1031–1035. https://doi.org/10.1038/ngeo1992

Lucazeau, F. (2019). Analysis and mapping of an updated terrestrial heat flow data set. *Geochemistry, Geophysics, Geosystems*, *20*, 4001–4024. https://doi.org/10.1029/2019GC008389

MacGregor, J. A., Fahnestock, M. A., Catania, G. A., Aschwanden, A., Clow, G. D., Colgan, W. T., et al. (2016). A synthesis of the basal thermal state of the Greenland Ice Sheet. *Journal of Geophysical Research: Earth Surface*, *121*, 1328–1350. https://doi.org/10.1002/2015JF003803

Maritati, A., Halpin, J. A., Whittaker, J. M., & Daczko, N. R. (2019). Fingerprinting Proterozoic bedrock in interior Wilkes Land, East Antarctica. *Scientific Reports*, *9*(1), 10192. https://doi.org/10.1038/s41598-019-46612-y

Martos, Y. M., Catalán, M., Jordan, T. A., Golynsky, A., Golynsky, D., Eagles, G., & Vaughan, D. G. (2017). Heat flux distribution of Antarctica unveiled. *Geophysical Research Letters*, *44*, 11417–11426. https://doi.org/10.1002/2017GL075609

Matsuoka, K., MacGregor, J. A., & Pattyn, F. (2012). Predicting radar attenuation within the Antarctic ice sheet. *Earth and Planetary Science Letters*, *359–360*, 173–183. https://doi.org/10.1016/j.epsl.2012.10.018

Maus, S., Barckhausen, U., Berkenbosch, H., Bournas, N., Brozena, J., Childers, V., et al. (2009). EMAG2: A 2-arc min resolution Earth Magnetic Anomaly Grid compiled from satellite, airborne, and marine magnetic measurements. *Geochemistry, Geophysics, Geosystems*, *10*, Q08005. https://doi.org/10.1029/2009GC002471

McKinney, W. (2015). *Pandas data analysis library*. Retrieved from http://pandas.pydata.org/

McLaren, S., Sandiford, M., Hand, M., Neumann, N., Wyborn, L., & Bastrakova, I. (2003). The hot southern continent: Heat flow and heat production in Australian Proterozoic terranes. *Special Paper of the Geological Society of America*, *372*, 157–167. https://doi.org/10.1130/0-8137-2372-8.157

Meyer, B., Saltus, R., & Chulliat, A. (2016). *EMAG2: Earth magnetic anomaly grid (2-arc-minute resolution) version 3*. Washington, DC: National Centers for Environmental Information, NOAA. Model, National Centers for Environmental Information, NOAA.

Mony, L., Roberts, J. L., & Halpin, J. A. (2020). Inferring geothermal heat flux from an ice-borehole temperature profile at Law Dome, East Antarctica. *Journal of Glaciology*, *66*(257), 509–519. https://doi.org/10.1017/jog.2020.27

Morin, R. H., Williams, T., Henrys, S. A., Magens, D., Niessen, F., & Hansaraj, D. (2010). Heat flow and hydrologic characteristics at the AND-1B borehole, ANDRILL McMurdo Ice Shelf project, Antarctica. *Geosphere*, *6*(4), 370–378. https://doi.org/10.1130/GES00512.1

Morlighem, M., Rignot, E., Binder, T., Blankenship, D., Drews, R., Eagles, G., et al. (2019). Deep glacial troughs and stabilizing ridges unveiled beneath the margins of the Antarctic ice sheet. *Nature Geoscience*, *13*, 132–137. https://doi.org/10.1038/s41561-019-0510-8

Morse, P. E., Reading, A. M., & Stål, T. (2019). Well-posed geoscientific visualization through interactive color mapping. *Frontiers of Earth Science*, *7*, 274. https://doi.org/10.3389/feart.2019.00274

Mouginot, J., Scheuchl, B., & Rignot, E. (2017). *MEaSUREs Antarctic Boundaries for IPY 2007–2009 from satellite radar, version 2*. Boulder, CO: NASA National Snow and Ice Data Center DAAC.

O'Donnell, J. P., Stuart, G. W., Brisbourne, A. M., Selway, K., Yang, Y., Nield, G. A., et al. (2019). The uppermost mantle seismic velocity structure of West Antarctica from Rayleigh wave tomography: Insights into tectonic structure and geothermal heat flow. *Earth and Planetary Science Letters*, *522*, 219–233. https://doi.org/10.1016/j.epsl.2019.06.024

Pail, R., Goiginger, H., Schuh, W. D., Hck, E., Brockmann, J. M., Fecher, T., et al. (2010). Combined satellite gravity field model GOCO01S derived from GOCE and GRACE. *Geophysical Research Letters*, *37*, L20314. https://doi.org/10.1029/2010GL044906

Pattyn, F. (2010). Antarctic subglacial conditions inferred from a hybrid ice sheet/ice stream model. *Earth and Planetary Science Letters*, *295*(3–4), 451–461. https://doi.org/10.1016/j.epsl.2010.04.025

Pattyn, F., Carter, S. P., & Thoma, M. (2016). Advances in modeling subglacial lakes and their interaction with the Antarctic ice sheet. *Philosophical Transactions of the Royal Society A: Mathematical, Physical & Engineering Sciences*, *374*(2059), 20140296. https://doi.org/10.1098/rsta.2014.0296

Paxman, G. J., Jamieson, S. S., Hochmuth, K., Gohl, K., Bentley, M. J., Leitchenkov, G., & Ferraccioli, F. (2019). Reconstructions of Antarctic topography since the EoceneOligocene boundary. *Palaeogeography, Palaeoclimatology, Palaeoecology*, *535*, 109346. https://doi.org/10.1016/j.palaeo.2019.109346

Pedregosa, F., Weiss, R., Brucher, M., Pedregosa, F., Pedregosa, F., Varoquaux, G., et al. (2011). Scikit-learn: Machine learning in Python. *Journal of Machine Learning Research*, *12*, 2825–2830.

Pérez-Díaz, L., Alcalde, J., & Bond, C. E. (2020). Introduction: Handling uncertainty in the geosciences: Identification, mitigation and communication. *Solid Earth*, *11*, 889–897. https://doi.org/10.5194/se-11-889-2020

Pittard, M. L., Galton-Fenzi, B. K., Roberts, J. L., & Watson, C. S. (2016). Organization of ice flow by localized regions of elevated geothermal heat flux. *Geophysical Research Letters*, *43*, 3342–3350. https://doi.org/10.1002/2016GL068436

Pollack, H. N., Hurter, S. J., & Johnson, J. R. (1993). Heat flow from the Earth's interior: Analysis of the global data set. *Reviews of Geophysics*, *31*(3), 267–280. https://doi.org/10.1029/93RG01249

Pollett, A., Hasterok, D., Raimondo, T., Halpin, J. A., Hand, M., Bendall, B., & McLaren, S. (2019). Heat flow in Southern Australia and connections with East Antarctica. *Geochemistry, Geophysics, Geosystems*, *20*, 5352–5370. https://doi.org/10.1029/2019GC008418

Price, P. B., Nagornov, O. V., Bay, R., Chirkin, D., He, Y., Miocinovic, P., et al. (2002). Temperature profile for glacial ice at the South Pole: Implications for life in a nearby subglacial lake. *Proceedings of the National Academy of Sciences of the United States of America*, *99*(12), 7844–7847. https://doi.org/10.1073/pnas.082238999

Purucker, M. (2012). Antarctica Basal Heat Flux: Geothermal heat flux data set based on low resolution observations collected by the CHAMP satellite between 2000 and 2010, and produced from the MF-6 model following the technique described in Fox Maule et al. (2005). *University of Montana*, *Oct*. http://websrv.cs.umt.edu/isis/index.php/Antarctica_Basal_Heat_Flux

Roy, S., & Rao, R. U. (2003). Toward a crustal thermal model for the Archean Dharwar craton, southern India. *Physics and Chemistry of the Earth*, *28*(9–11), 361–373. https://doi.org/10.1016/S1474-7065(03)00058-5

Rudnick, R., & Nyblade, A. (1999). The thickness and heat production of Archean lithosphere: Constraints from xenolith thermobarometry and surface heat flow. *Mantle Petrology: Field Observations and High Pressure Experimentation: A Tribute to Francis R. (Joe) Boyd*, *6*(6), 3–12.

Ruppel, A., Jacobs, J., Eagles, G., Läufer, A., & Jokat, W.. (2018). New geophysical data from a key region in East Antarctica: Estimates for the spatial extent of the Tonian Oceanic Arc Super Terrane (TOAST). *Gondwana Research*, *59*, 97–107. https://doi.org/10.1016/j.gr.2018.02.019

Sauermilch, I., Whittaker, J. M., Bijl, P. K., Totterdell, J. M., & Jokat, W. (2019). Tectonic, Oceanographic, and climatic controls on the Cretaceous-Cenozoic Sedimentary Record of the Australian-Antarctic Basin. *Journal of Geophysical Research: Solid Earth*, *124*, 7699–7724. https://doi.org/10.1029/2018JB016683

Schaeffer, A. J., & Lebedev, S. (2015). Global heterogeneity of the lithosphere and underlying mantle: A seismological appraisal based on multimode surface-wave dispersion analysis, shear-velocity tomography, and tectonic regionalization. In A. Khan, & F. Deschamps (Eds.), *The earth's heterogeneous mantle: A geophysical, geodynamical, and geochemical perspective* (pp. 3–46). Charm: Springer International Publishing. https://doi.org/10.1007/978-3-319-15627-9_1

Scheinert, M., Ferraccioli, F., Schwabe, J., Bell, R., Studinger, M., Damaske, D., et al. (2016). New Antarctic gravity anomaly grid for enhanced geodetic and geophysical studies in Antarctica. *Geophysical Research Letters*, *43*, 600–610. https://doi.org/10.1002/2015GL067439

Schroeder, D. M., Blankenship, D. D., Young, D. A., & Quartini, E. (2014). Evidence for elevated and spatially variable geothermal flux beneath the West Antarctic Ice Sheet. *Proceedings of the National Academy of Sciences of the United States of America*, *111*(25), 9070–9072. https://doi.org/10.1073/pnas.1405184111

Shannon, C. E.. (1948). A mathematical theory of communication. *Bell System Technical Journal*, *27*(3), 379–423. https://doi.org/10.1002/j.1538-7305.1948.tb01338.x

Shapiro, N. M., & Ritzwoller, M. H. (2004). Inferring surface heat flux distributions guided by a global seismic model: Particular application to Antarctica. *Earth and Planetary Science Letters*, *223*(1–2), 213–224.doi https://doi.org/10.1016/j.epsl.2004.04.011

Shen, W., Wiens, D. A., Anandakrishnan, S., Aster, R. C., Gerstoft, P., Bromirski, P. D., et al. (2018). The crust and upper mantle structure of Central and West Antarctica from Bayesian inversion of Rayleigh wave and receiver functions. *Journal of Geophysical Research: Solid Earth*, *123*, 7824–7849. https://doi.org/10.1029/2017JB015346

Shen, W., Wiens, D. A., Lloyd, A. J., & Nyblade, A. A. A. (2020). A geothermal heat flux map of Antarctica empirically constrained by seismic structure. *Geophysical Research Letters*, *47*, e2020GL086955. https://doi.org/10.1029/2020GL086955

Siegert, M. J., Ross, N., & Le Brocq, A. M. (2016). Recent advances in understanding Antarctic subglacial lakes and hydrology. *Philosophical Transactions of the Royal Society A: Mathematical, Physical & Engineering Sciences*, *374*(2059), 20140306. https://doi.org/10.1098/rsta.2014.0306

Sinem Ince, E., Barthelmes, F., Reißland, S., Elger, K., Förste, C., Flechtner, F., & Schuh, H. (2019). ICGEM 15 years of successful collection and distribution of global gravitational models, associated services, and future plans. *Earth System Science Data*, *11*(2), 647–674. https://doi.org/10.5194/essd-11-647-2019

Snow, A. D., Whitaker, J., Cochran, M., Bossche, J. V. d., Mayo, C., Kloe, J. D., et al. (2020). *pyproj4/pyproj: 2.6.0 Release. Zenodo*. https://doi.org/10.5281/zenodo.3714221

Stål, T., Reading, A. M., Halpin, J. A., Steven, J. P., & Whittaker, J. M. (2020). The Antarctic crust and upper mantle: A flexible 3D model and framework for interdisciplinary research. *Frontiers in Earth Science*. *8*, 447. https://doi.org/10.3389/feart.2020.577502

Stål, T., & Reading, A. M. (2020). A grid for multidimensional and multivariate spatial representation and data processing. *Journal of Open Research Software*, *8*(1), 1–10. https://doi.org/10.5334/JORS.287

Stål, T., Reading, A. M., Halpin, J. A., & Whittaker, J. M. (2019). A multivariate approach for mapping lithospheric domain boundaries in East Antarctica. *Geophysical Research Letters*, *46*(17–18), 10404–10416. https://doi.org/10.1029/2019GL083453

Stål, T., Reading, A. M., Halpin, J. A., & Whittaker, J. (2020). Dataset: Antarctic geothermal heat flow model: Aq1. *PANGAEA*. https://doi.org/10.1594/PANGAEA.924857

Szwillus, W., Afonso, J. C., Ebbing, J., & Mooney, W. D. (2019). Global crustal thickness and velocity structure from geostatistical analysis of seismic data. *Journal of Geophysical Research: Solid Earth*, *124*, 1626–1652. https://doi.org/10.1029/2018JB016593

Tingey, R. J., Swoboda, R., & Gallagher, J. (1991). *Schematic geological map of Antarctica*. Bureau of Mineral Resources, Geology and Geophysics, Department of Primary Industries and Energy.

Tooze, S., Halpin, J. A., Noble, T. L., Chase, Z., O'Brien, P. E., & Armand, L. (2020). Scratching the surface: A marine sediment provenance record from the continental slope of central Wilkes Land, East Antarctica. *Geochemistry, Geophysics, Geosystems*, *21*, e2020GC009156. https://doi.org/10.1029/2020GC009156

Tucker, N. M., Payne, J. L., Clark, C., Hand, M., Taylor, R. J., Kylander-Clark, A. R., & Martin, L. (2017). Proterozoic reworking of Archean (Yilgarn) basement in the Bunger Hills, East Antarctica. *Precambrian Research*, *298*, 16–38. https://doi.org/10.1016/j.precamres.2017.05.013

Tulaczyk, S. M., Scherer, R. P., & Clark, C. D. (2001). A plowing model for the origin of weak tills beneath ice streams: A qualitative treatment. *Quaternary International*, *86*(1), 59–70. https://doi.org/10.1016/s1040-6182(01)00050-7

Van Liefferinge, B., Pattyn, F., Cavitte, M. G., Karlsson, N. B., Young, D. A., Sutter, J., & Eisen, O. (2018). Promising oldest ice sites in east Antarctica based on thermodynamical modeling. *The Cryosphere*, *12*(8), 2773–2787. https://doi.org/10.5194/tc-12-2773-2018

van Wyk de Vries, M., Bingham, R. G., & Hein, A. S. (2018). A new volcanic province: An inventory of subglacial volcanoes in West Antarctica. *Geological Society Special Publication*, *461*(1), 231–248. https://doi.org/10.1144/SP461.7

Waskom, M., Botvinnik, O., Ostblom, J., Lukauskas, S., Hobson, P., Maoz, Gelbart, et al. (2020). mwaskom/seaborn: v0.10.0 (January 2020). *Zenodo*. https://doi.org/10.5281/ZENODO.592845

Wellmann, J. F., & Regenauer-Lieb, K. (2012). Uncertainties have a meaning: Information entropy as a quality measure for 3-D geological models. *Tectonophysics*, *526–529*, 207–216. https://doi.org/10.1016/j.tecto.2011.05.001

Whitehouse, P. L., Gomez, N., King, M. A., & Wiens, D. A. (2019). Solid Earth change and the evolution of the Antarctic Ice Sheet. *Nature Communications*, *10*(1), 503. https://doi.org/10.1038/s41467-018-08068-y

Wilson, D. S., Jamieson, S. S., Barrett, P. J., Leitchenkov, G., Gohl, K., & Larter, R. D.. (2012). Antarctic topography at the Eocene-Oligocene boundary. *Paleogeography, Paleoclimatology, Palaeoecology*, *335–336*, 24–34. https://doi.org/10.1016/j.palaeo.2011.05.028

Winkelmann, R., Martin, M. A., Haseloff, M., Albrecht, T., Bueler, E., Khroulev, C., & Levermann, A. (2011). The Potsdam Parallel Ice Sheet Model (PISM-PIK)—Part 1: Model description. *The Cryosphere*, *5*(3), 715–726. https://doi.org/10.5194/tc-5-715-2011

Wright, R., & Pilger, E. (2008). Radiant flux from Earth's subaerially erupting volcanoes. *International Journal of Remote Sensing*, *29*(22), 6443–6466. https://doi.org/10.1080/01431160802168210

Wright, A. P., Young, D. A., Roberts, J. L., Schroeder, D. M., Bamber, J. L., Dowdeswell, J. A.,et al. (2012). Evidence of a hydrological connection between the ice divide and ice sheet margin in the Aurora Subglacial Basin, East Antarctica. *Journal of Geophysical Research*, *117*, F01033. https://doi.org/10.1029/2011JF002066

Reference From the Supporting Information

Salmon, M., Kennett, B. L., Stern, T., & Aitken, A. R. (2013). The Moho in Australia and New Zealand. *Tectonophysics*, *609*, 288–298. https://doi.org/10.1016/j.tecto.2012.07.009